

Complete synthetic seismograms based on a spherical self-gravitating Earth model with an atmosphere–ocean–mantle–core structure

Rongjiang Wang,¹ Sebastian Heimann,¹ Yong Zhang,² Hansheng Wang³
 and Torsten Dahm¹

¹Helmholtz Centre Potsdam, GFZ German Research Centre for Geosciences, D-14473 Potsdam, Germany. E-mail: wang@gfz-potsdam.de

²School of Earth and Space Sciences, Peking University, Beijing 100871, China

³State Key Laboratory of Geodesy and Earth's Dynamics, Institute of Geodesy and Geophysics, Chinese Academy of Sciences, Wuhan 430077, China

Accepted 2017 June 13. Received 2017 June 9; in original form 2016 November 23

SUMMARY

A hybrid method is proposed to calculate complete synthetic seismograms based on a spherically symmetric and self-gravitating Earth with a multilayered structure of atmosphere, ocean, mantle, liquid core and solid core. For large wavelengths, a numerical scheme is used to solve the geodynamic boundary-value problem without any approximation on the deformation and gravity coupling. With decreasing wavelength, the gravity effect on the deformation becomes negligible and the analytical propagator scheme can be used. Many useful approaches are used to overcome the numerical problems that may arise in both analytical and numerical schemes. Some of these approaches have been established in the seismological community and the others are developed for the first time. Based on the stable and efficient hybrid algorithm, an all-in-one code QSSP is implemented to cover the complete spectrum of seismological interests. The performance of the code is demonstrated by various tests including the curvature effect on teleseismic body and surface waves, the appearance of multiple reflected, teleseismic core phases, the gravity effect on long period surface waves and free oscillations, the simulation of near-field displacement seismograms with the static offset, the coupling of tsunami and infrasound waves, and free oscillations of the solid Earth, the atmosphere and the ocean. QSSP is open source software that can be used as a stand-alone FORTRAN code or may be applied in combination with a Python toolbox to calculate and handle Green's function databases for efficient coding of source inversion problems.

Key words: Acoustic-gravity waves; Body waves; Computational seismology; Surface waves and free oscillations; Theoretical seismology; Wave propagation.

1 INTRODUCTION

The efficient calculation of complete wave fields of displacement, tilt, strain or stress in a broad frequency band (e.g. from dc to 2 Hz), generated by point sources in different layers of the Earth, is still of great scientific interest, although different solutions have been presented in the past for specific wave modes or frequency ranges. The geodynamic boundary-value problem can be solved based on a spherically symmetric Earth model, for which semi-analytical solutions are available. In many cases, the semi-analytical solutions are sufficiently accurate for interpreting the observations. In other cases, they can provide a good reference for heterogeneous 3-D Earth models.

The semi-analytical solutions are commonly obtained with the spectral method. Making a Fourier (Laplace) transform with respect to the time variable and expanding the frequency-domain observables (displacement-stress vector) into spherical harmonics, the partial differential equations of motion are converted to a set of ordinary differential equations governing the spectral observables as functions of radius (depth). The latter can be solved using either the propagator or numerical integration approach, depending on whether all fundamental solutions exist for each homogeneous spherical shell. The time–space domain solutions are obtained finally by the summation of weighted spherical harmonics and inverse Fourier (Laplace) transform.

For seismological applications, there have been various semi-analytical modelling tools based on spherical Earth models. Some of them were developed to calculate the static deformation and gravity changes caused by dislocation sources (Pollitz 1992, 1997; Okubo 1993; Sun & Okubo 1993, 1998). These tools differ mainly in whether an analytical propagator or a numerical integration approach is used to solve the ordinary differential equations. In order to model seismic deformation at local to regional scales, the corresponding tools based on the half-space geometry were developed in parallel to those based on the spherical geometry. For example, the analytical closed-form

dislocation model based on a homogeneous elastic half-space (Okada 1992) is most widely used to analyse near-field geodetic observations. For large-scale earthquakes whose deformation field may be modified by the structure below the seismogenic zone, the semi-analytical tools based on a multilayered elastic or viscoelastic half-space are often used (Rundle 1980, 1981, 1982; Wang *et al.* 2003, 2006).

The other tools, which are in the interest of this paper, are those for generating complete synthetic seismograms, such as the reflectivity method (Fuchs 1968; Fuchs & Müller 1971; Kennett 1983; Müller 1985) or the orthonormal propagator method (Chapman & Phinney 1972; Wang 1999; Chapman 2003) with improved computational efficiency. Here, it is important to recognize that nearly complete seismograms at teleseismic distances on a spherical Earth can also be generated using a layered half-space model by applying the so-called earth-flattening transformation (Müller 1985) to the seismic material parameters. However, this approximation usually breaks down for very large distances ($\geq 120^\circ$) and for rays with turning points in the inner core.

Many corresponding tools for synthetic seismograms have been developed recently based on spherical Earth models (Friederich & Dalkolmo 1995; Kawai *et al.* 2006; Al-Attar & Woodhouse 2008; Yang *et al.* 2010; Masters *et al.* 2011; van Driel *et al.* 2015). We mention two of them that are widely used currently in the seismological community: MINEOS written by Masters *et al.* (2011) and GEMINI written by Friederich & Dalkolmo (1995). MINEOS calculates eigenfrequencies and eigenfunctions of a spherically symmetric and self-gravitating Earth model (Gilbert & Backus 1966, 1968) and then generate low-frequency (≤ 0.15 Hz) seismograms through the normal mode summation. As a complementary to MINEOS, GEMINI uses the frequency-domain integration method, which is recommended to calculate complete synthetic seismograms at higher frequency (up to 1–2 Hz).

In mathematics, the spectral methods applied to the spherical and half-space geometries differ in the way that the former uses a discrete series of spherical harmonics and the latter uses a continuous spectrum of cylindrical harmonics to represent the spatial variations of observables. Under certain assumptions, the time-space-domain results from any two corresponding spherical and half-space models are in principle comparable. Cross checks between them are useful to find bugs and clarify limitations existing in different program codes.

It is recognized that also the semi-analytical tools may involve different numerical problems. In particular, unstable results may be caused by (1) degeneration of fundamental solutions at the dynamic-to-static transition and in other extreme cases, (2) the effect of the Brunt–Väisälä (buoyancy) frequency existing in the liquid core, ocean and atmosphere, (3) loss of precision when using the traditional propagator algorithm at short wavelengths, (4) slow convergence when the source and receiver are located at close depths and (5) time-domain and space-domain aliasing. Though there have been many techniques to overcome these numerical difficulties, they are not systematically implemented in the existing tools mentioned above. Moreover, the different tools were developed for specific purposes with some limitations. For example, though static deformation can be determined directly from the permanent offset of a complete displacement seismogram, it often needs to be calculated with an independent static dislocation tool because of numerical efficiency and stability. Besides, complete synthetic seismograms are almost always generated for a solid Earth and therefore they generally do not include oceanic tsunami and atmospheric acoustic-infrasound waves.

In this paper we present a new method to calculate complete seismograms based on a non-rotating, spherically symmetric, isotropic linear elastic and self-gravitating Earth with a multilayered structure of the atmosphere, ocean, mantle, liquid core and solid core. The term ‘complete’ means that all seismic signals, which exist physically for the assumed model and are numerically significant at the spatial and temporal scales selected by users, are included with sufficient accuracy. In this case, it includes static offset, free oscillations of the solid Earth and the atmosphere and the ocean, body and surface waves, tsunami and acoustic-infrasound waves, etc. Based on this method, an all-in-one code, called QSSP, was implemented and has been updated several times over last few years. Actually, the performance of QSSP has been tested with GEMINI (Friederich & Dalkolmo 1995) and QSEIS (Wang 1999). The current version of QSSP is used routinely for generating Green’s function databases for seismic source inversion (e.g. Heimann *et al.* 2013; Schurr *et al.* 2014; Zhang *et al.* 2014a,b). Other applications of QSSP are demonstrated, for example, by Ivan & Wang (2013) and Ivan *et al.* (2015) for comparison of observed seismic phases Pdif and P5KP with their synthetics, and by Raveloson *et al.* (2012) for simulating infrasound gravity waves induced by the great 2004 Indian Ocean tsunami. Further application examples and cross checks with other tools are demonstrated in this paper after a comprehensive introduction to the basic theory and a detailed description of the algorithm used in QSSP. The new methods can be used by scientists and seismologists for the modelling of wave fields or the inversion of seismic sources in the Earth or in other planets, but it is also recommended for routine automatic applications because of its efficiency and robustness.

2 THEORY

In this study, we are interested in the complete deformation process induced by an earthquake in a spherically symmetric, elastic and self-gravitating Earth. The equations of motion governing the geodynamic process are described in the Appendix. By means of the Fourier (Laplace) transform and the spherical harmonic expansion, the partial differential equations of motion are converted to two sets of first-order ordinary differential equations governing the unknowns that depend only on the radius from the centre of the Earth. One set consists of six equations governing the spheroidal mode of motion (*P*–*SV* waves) that is coupled with the gravity field, whereas the other set consists of two equations governing the toroidal mode of motion (*SH* waves) that is decoupled from the gravity field. Once the frequency-wavelength domain solutions are calculated, the time–space domain solutions can be obtained through summation of the spherical harmonic terms and then the inverse Fourier (Laplace) transform.

For a homogeneous spherical shell, Gilbert & Backus (1968) derived the analytical closed-form solutions for both spheroidal and toroidal modes. However, their analytical spheroidal solutions were obtained under the assumption that the gravity is proportional to the radius, that is $g(rr)/r = \text{const}$. For a stratified Earth structure, this assumption is only realistic within the core. The complete analytical solutions without the influence of the gravity on the deformation field were presented by Takeuchi & Saito (1972).

Since the gravity effect is significant only for very large wavelengths, that is for long-period and low-degree free oscillations, we suggest a hybrid algorithm, in which the long-wavelength spheroidal modes are solved using the numerical Runge–Kutta integration of the equations given in the Appendix, while the small-wavelength spheroidal modes and the complete toroidal modes are solved using the analytical Haskell propagator method.

In the following subsections, we firstly summarize the fundamental toroidal and spheroidal solutions adopted from Takeuchi & Saito (1972). Then, we show the degeneration problems that may arise not only at the static limit but also in the case if the viscoelastic attenuation is considered. One of these degeneration problems (degeneration of the converging pair of spheroidal modes) was solved already by Takeuchi & Saito (1972). We present, for the first time, the solutions for all remaining degeneration problems. Finally, we derived the Haskell propagator for the layered spherical structure in a form similar to that used in the reflectivity method for the layered half-space structure.

2.1 Analytical toroidal solutions (*SH* waves) in a homogeneous spherical shell

The toroidal mode is described by a 2-D displacement–stress vector, which is denoted by $\mathbf{x} = (X_1, rX_2)^T$ in the frequency–wavenumber domain (the Appendix). There are two fundamental toroidal solutions ($\mathbf{x}_1, \mathbf{x}_2$) in a homogeneous spherical shell, referred to as the converging and diverging *SH* waves, which can be expressed in the analytical closed forms (Takeuchi & Saito 1972),

$$\begin{cases} X_{11} = j_l(x_s), \\ rX_{21} = \mu [(l-1)j_l(x_s) - x_s j_{l+1}(x_s)], \end{cases} \quad (1)$$

and

$$\begin{cases} X_{12} = y_l(x_s), \\ rX_{22} = \mu [(l-1)y_l(x_s) - x_s y_{l+1}(x_s)], \end{cases} \quad (2)$$

respectively, where

$$x_s = k_s r = \frac{\omega}{V_s} r, \quad (3)$$

μ is the second Lamé constant (also called the shear modulus), V_s is the *S*-wave velocity, ω is the angular frequency, r is the radius of the spherical shell, $k_s = \frac{\omega}{V_s}$ is the wavenumber, and $j_l(x)$ and $y_l(x)$ are the spherical Bessel functions of degree l of the first and second kind, respectively.

2.2 Analytical spheroidal solutions (*P–SV* waves) in a homogeneous spherical shell

For deformation of small wavelengths, the gravity effect is negligible. In this case, we consider a hierarchical deformation–gravity coupling, that is the gravity depends on the mass redistribution induced by the deformation, but the deformation is decoupled from the gravity. Mathematically, we delete the second and third terms on the right hand side of the first equation of eq. (A1) in the Appendix, but describe the spheroidal motion still by a 6-D displacement–stress vector, which is denoted by $\mathbf{y} = (rY_1, r^2Y_2, rY_3, r^2Y_4, Y_5, rY_6)^T$ in the frequency–wavenumber domain. Within a homogeneous shell, there are six fundamental spheroidal solutions ($\mathbf{y}_1, \mathbf{y}_2, \mathbf{y}_3, \mathbf{y}_4, \mathbf{y}_5, \mathbf{y}_6$), which were derived by Takeuchi & Saito (1972). The first pair of spheroidal solutions, which make up the converging and diverging *P* waves, respectively, are expressed in the analytical closed forms,

$$\begin{cases} rY_{11} = l j_l(x_p) - x_p j_{l+1}(x_p), \\ r^2 Y_{21} = -(\lambda + 2\mu)x_p^2 j_l(x_p) + 2\mu [l(l-1)j_l(x_p) + 2x_p j_{l+1}(x_p)], \\ rY_{31} = j_l(x_p), \\ r^2 Y_{41} = 2\mu [(l-1)j_l(x_p) - x_p j_{l+1}(x_p)], \\ Y_{51} = 4\pi G\rho j_l(x_p), \\ rY_{61} = 4\pi G\rho (l+1)j_l(x_p), \end{cases} \quad (4)$$

and

$$\begin{cases} rY_{12} = ly_l(x_p) - x_p y_{l+1}(x_p), \\ r^2 Y_{22} = -(\lambda + 2\mu)x_p^2 y_l(x_p) + 2\mu[l(l-1)y_l(x_p) + 2x_p y_{l+1}(x_p)], \\ rY_{32} = y_l(x_p), \\ r^2 Y_{42} = 2\mu[(l-1)y_l(x_p) - x_p y_{l+1}(x_p)], \\ Y_{52} = 4\pi G\rho y_l(x_p), \\ rY_{62} = 4\pi G\rho(l+1)y_l(x_p), \end{cases} \quad (5)$$

where

$$x_p = k_p r = \frac{\omega}{V_p} r, \quad (6)$$

V_p is the P -wave velocity, λ is the first Lamé constant, ρ is the density, G is the gravitational constant and $k_p = \frac{\omega}{V_p}$ is the P wavenumber. The second pair of spheroidal solutions making up the converging and diverging SV waves are

$$\begin{cases} rY_{13} = -l(l+1)j_l(x_s), \\ r^2 Y_{23} = 2\mu l(l+1)[-(l-1)j_l(x_s) + x_s j_{l+1}(x_s)], \\ rY_{33} = -(l+1)j_l(x_s) + x_s j_{l+1}(x_s), \\ r^2 Y_{43} = \mu[x_s^2 j_l(x_s) - 2(l^2 - 1)j_l(x_s) - 2x_s j_{l+1}(x_s)], \\ Y_{53} = 0, \\ rY_{63} = 4\pi G\rho l(l+1)j_l(x_s), \end{cases} \quad (7)$$

and

$$\begin{cases} rY_{14} = -l(l+1)y_l(x_s), \\ r^2 Y_{24} = 2\mu l(l+1)[-(l-1)y_l(x_s) + x_s y_{l+1}(x_s)], \\ rY_{34} = -(l+1)y_l(x_s) + x_s y_{l+1}(x_s), \\ r^2 Y_{44} = \mu[x_s^2 y_l(x_s) - 2(l^2 - 1)y_l(x_s) - 2x_s y_{l+1}(x_s)]. \\ Y_{54} = 0, \\ rY_{64} = 4\pi G\rho l(l+1)y_l(x_s). \end{cases} \quad (8)$$

The third pair of spheroidal solutions describe the case in which no deformation is caused and the gravity potential is harmonic in the spherical shell. One of these solutions is regular at $r = 0$,

$$\begin{cases} rY_{15} = 0, \\ r^2 Y_{25} = 0, \\ rY_{35} = 0, \\ r^2 Y_{45} = 0, \\ Y_{55} = r^l, \\ rY_{65} = (2l+1)r^l, \end{cases} \quad (9)$$

and the other is singular at $r = 0$,

$$\begin{cases} rY_{16} = 0, \\ r^2 Y_{26} = 0, \\ rY_{36} = 0, \\ r^2 Y_{46} = 0, \\ Y_{56} = r^{-(l+1)}, \\ rY_{66} = 0. \end{cases} \quad (10)$$

2.3 Underflow, overflow and degeneration at the static limit

At very low frequency ($\omega \rightarrow 0$) or when $l \gg |x_s| > |x_p|$, underflow and overflow can arise for numerical computations of the spherical Bessel functions $j_l(x)$ and $y_l(x)$, respectively. In this case, we reformulate the fundamental solutions using the method suggested by Takeuchi & Saito (1972). If $l > |x_s|^2/2 \geq |x_p|^2/2$, the two spherical Bessel functions can be replaced by their asymptotic expansion series,

$$\phi_l(x) = \frac{(2l+1)!!}{x^l} j_l(x) = 1 - \frac{x^2}{2^1 (2l+3) \cdot 1!} + \frac{x^4}{2^2 (2l+3)(2l+5) \cdot 2!} - \dots, \quad (11)$$

and

$$\varphi_l(x) = \frac{x^{l+1}}{(2l-1)!!} y_l(x) = 1 + \frac{x^2}{2^1 (2l-1) \cdot 1!} + \frac{x^4}{2^2 (2l-1)(2l-3) \cdot 2!} + \dots, \quad (12)$$

respectively, where $n!!$ denotes the semi-factorial of n , for example, $(2l+1)!! = 1 \cdot 3 \cdot 5 \cdots (2l+1)$ and $(2l)!! = 2 \cdot 4 \cdot 6 \cdots (2l)$. Note that some typos in the Takeuchi & Saito (1972) expression for $\phi_l(x)$ have been corrected. Accordingly, if $l > |x_s|^2/2$, we multiply eqs (1) and (2) with the constant factors $(2l+1)!!/k_s^l$ and $-k_s^{l+1}/(2l-1)!!$ and obtain

$$\begin{cases} X_{11} = r^l \phi_l(x_s), \\ rX_{21} = r^l \mu \left[(l-1) \phi_l(x_s) - \frac{x_s^2}{2l+3} \phi_{l+1}(x_s) \right], \end{cases} \quad (1a)$$

and

$$\begin{cases} X_{12} = r^{-(l+1)} \varphi_l(x_s), \\ rX_{22} = r^{-(l+1)} \mu [(l-1) \varphi_l(x_s) - (2l+1) \varphi_{l+1}(x_s)], \end{cases} \quad (2a)$$

respectively. It is interesting to see that in the static case, that is when $\omega = 0$, the two toroidal solutions are expressed in the following simple form,

$$\begin{cases} X_{11} = r^l, \\ rX_{21} = (l-1) \mu r^l, \end{cases} \quad (1b)$$

and

$$\begin{cases} X_{12} = r^{-(l+1)}, \\ rX_{22} = -(l+2) \mu r^{-(l+1)}, \end{cases} \quad (2b)$$

respectively. These static toroidal solutions are identical with those given by Pollitz (1992).

For the same reason, the spheroidal solutions need to be reformulated at very low frequency or for very large harmonic degrees. For $l > |x_p|^2/2$, we can use

$$\begin{cases} rY_{11} = r^l \left[l\phi_l(x_p) - \frac{x_p^2 \phi_{l+1}(x_p)}{(2l+3)} \right], \\ r^2 Y_{21} = r^l \left\{ [-(\lambda + 2\mu)x_p^2 + 2\mu l(l-1)]\phi_l(x_p) + \frac{4\mu x_p^2 \phi_{l+1}(x_p)}{(2l+3)} \right\}, \\ rY_{31} = r^l \phi_l(x_p), \\ r^2 Y_{41} = 2\mu r^l \left[(l-1)\phi_l(x_p) - \frac{x_p^2 \phi_{l+1}(x_p)}{(2l+3)} \right], \\ Y_{51} = 4\pi G\rho r^l \phi_l(x_p), \\ rY_{61} = 4\pi G\rho r^l (l+1)\phi_l(x_p), \end{cases} \quad (4a)$$

and

$$\begin{cases} rY_{12} = r^{-(l+1)} \left[-(l+1)\varphi_l(x_p) + \frac{x_p^2\varphi_{l-1}(x_p)}{(2l-1)} \right], \\ r^2Y_{22} = r^{-(l+1)} \left\{ [-(\lambda+2\mu)x_p^2 + 2\mu(l+1)(l+2)]\varphi_l(x_p) - 4\mu \frac{x_p^2\varphi_{l-1}(x_p)}{(2l-1)} \right\}, \\ rY_{32} = r^{-(l+1)}\varphi_l(x_p), \\ r^2Y_{42} = 2\mu r^{-(l+1)} \left[-(l+2)\varphi_l(x_p) + \frac{x_p^2\varphi_{l-1}(x_p)}{(2l-1)} \right], \\ Y_{52} = 4\pi G\rho r^{-l+1}\varphi_l(x_p), \\ rY_{62} = 4\pi G\rho r^{-(l+1)}(l+1)\varphi_l(x_p), \end{cases} \quad (5a)$$

in place of eqs (4) and (5), respectively.

In principle, eqs (7) and (8) for the third and fourth spheroidal solutions in terms of x_s can be reformulated to the form similar to eqs (4a) and (5a), respectively. However, we find that when x_p and $x_s \rightarrow 0$, the third and fourth spheroidal solutions become linearly dependent with the first and second spheroidal solutions, respectively. This kind of degeneration was not considered by Takeuchi & Saito (1972). Here we solve the problem by making the linear combination [(4) · $(2l+1)!!/k_p^l$ + (7) · $(2l+1)!!/k_s^l/(l+1)$ − (9) · $4\pi G\rho$] · $[-2(2l+3)/k_s^2]$, resulting in a reformulated spheroidal solution in place of eq. (7),

$$\begin{cases} rY_{13} = r^{l+2} [l\eta\delta_l(x_p, x_s) - 2\xi\phi_{l+1}(x_p)], \\ r^2Y_{23} = 2\mu r^{l+2} [l(l-1)\eta\delta_l(x_p, x_s) - (2l+3)\phi_l(x_p) + 4\xi\phi_{l+1}(x_p) + 2l\phi_{l+1}(x_s)], \\ rY_{33} = r^{l+2} \left[\eta\delta_l(x_p, x_s) + \frac{2\phi_{l+1}(x_s)}{(l+1)} \right], \\ r^2Y_{43} = 2\mu r^{l+2} \left[(l-1)\eta\delta_l(x_p, x_s) - 2\xi\phi_{l+1}(x_p) + \frac{(2l+3)\phi_l(x_s) - 2\phi_{l+1}(x_s)}{(l+1)} \right], \\ Y_{53} = -4\pi G\rho r^{l+2}\xi\beta_l(x_p), \\ rY_{63} = 4\pi G\rho r^{l+2} \{(l+1)\eta\delta_l(x_p, x_s) - (2l+1)\beta_l(x_s)\}, \end{cases} \quad (7a)$$

where

$$\xi = \left(\frac{V_s}{V_p} \right)^2 = \frac{\mu}{\lambda + 2\mu}, \quad (13)$$

$$\eta = 1 - \xi = \frac{\lambda + \mu}{\lambda + 2\mu}, \quad (14)$$

$$\phi_l(x_p, x_s) = -2(2l+3) \frac{\phi_l(x_p) - \phi_l(x_s)}{x_p^2 - x_s^2} = 1 - \frac{x_p^2 + x_s^2}{2^1(2l+5) \cdot 2!} + \frac{x_p^4 + x_p^2x_s^2 + x_s^4}{2^2(2l+5)(2l+7) \cdot 3!} - \dots, \quad (15)$$

$$\beta_l(x) = -2(2l+3) \frac{\phi_l(x) - 1}{x^2} = 1 - \frac{x^2}{2^1(2l+5) \cdot 2!} + \frac{x^4}{2^2(2l+5)(2l+7) \cdot 3!} - \dots \quad (16)$$

Similarly, the fourth spheroidal solution can be reformulated using the linear combination [(5) · $k_p^{l+1}l/(2l-1)!!$ − (8) · $k_s^{l+1}/(2l-1)!!$ + (10) · $4\pi G\rho l$] · $[-2(2l-1)/k_s^2]$,

$$\begin{cases} rY_{14} = r^{-(l-1)} [l(l+1)\eta\varepsilon_l(x_p, x_s) + 2l\xi\varphi_{l-1}(x_p)], \\ r^2Y_{24} = 2\mu r^{-(l-1)}l [-(l+1)(l+2)\eta\varepsilon_l(x_p, x_s) - (2l-1)\phi_l(x_p) - 4\xi\varphi_{l-1}(x_p) + 2(l+1)\varphi_{l-1}(x_s)], \\ rY_{34} = r^{-(l-1)} [-l\eta\varepsilon_l(x_p, x_s) + 2\varphi_{l-1}(x_s)], \\ r^2Y_{44} = 2\mu r^{-(l-1)} [l(l+2)\eta\varepsilon_l(x_p, x_s) + 2l\xi\varphi_{l-1}(x_p) - (2l-1)\phi_l(x_s) - 2\varphi_{l-1}(x_s)], \\ Y_{54} = 4\pi G\rho r^{-(l-1)}l\xi\gamma_l(x_p), \\ rY_{64} = -4\pi G\rho r^{-(l-1)}l(l+1)\eta\varepsilon_l(x_p, x_s), \end{cases} \quad (8a)$$

where

$$\varepsilon_l(x_p, x_s) = 2(2l-1) \frac{\varphi_l(x_p) - \varphi_l(x_s)}{x_p^2 - x_s^2} = 1 + \frac{x_p^2 + x_s^2}{2^1(2l-3) \cdot 2!} + \frac{x_p^4 + x_p^2 x_s^2 + x_s^4}{2^2(2l-3)(2l-5) \cdot 3!} + \dots, \quad (17)$$

$$\gamma_l(x) = 2(2l-1) \frac{\varphi_l(x) - 1}{x^2} = 1 + \frac{x^2}{2^1(2l-3) \cdot 2!} + \frac{x^4}{2^2(2l-3)(2l-5) \cdot 3!} + \dots, \quad (18)$$

In the static case, that is for $\omega = 0$, all functions $\phi_l, \varphi_l, \delta_l, \beta_l, \varepsilon_l, \gamma_l$ and σ_l , as defined above, converge to 1. Consequently, all fundamental spheroidal solutions given by eqs (4a), (5a), (7a) and (8a) can be expressed in the following closed form,

$$\begin{cases} rY_{11} = lr^l, \\ r^2Y_{21} = 2\mu l(l-1)r^l, \\ rY_{31} = r^l, \\ r^2Y_{41} = 2\mu(l-1)r^l, \\ Y_{51} = 4\pi G\rho r^l, \\ rY_{61} = 4\pi G\rho(l+1)r^l, \end{cases} \quad (4b)$$

$$\begin{cases} rY_{12} = -(l+1)r^{-(l+1)}, \\ r^2Y_{22} = 2\mu(l+1)(l+2)r^{-(l+1)}, \\ rY_{32} = r^{-(l+1)}, \\ r^2Y_{42} = -2\mu(l+2)r^{-(l+1)}, \\ Y_{52} = 4\pi G\rho r^{-(l+1)}, \\ rY_{62} = 4\pi G\rho(l+1)r^{-(l+1)}, \end{cases} \quad (5b)$$

$$\begin{cases} rY_{13} = [l\eta - 2\xi]r^{l+2}, \\ r^2Y_{23} = 2\mu[l(l-1)\eta + 4\xi - 3]r^{l+2}, \\ rY_{33} = \left[\eta + \frac{2}{l+1}\right]r^{l+2}, \\ r^2Y_{43} = 2\mu\left\{(l-1)\eta - 2\xi + \frac{2l+1}{l+1}\right\}r^{l+2}, \\ Y_{53} = -4\pi G\rho\xi r^{l+2}, \\ rY_{63} = 4\pi G\rho[(l+1)\eta - (2l+1)]r^{l+2}, \end{cases} \quad (7b)$$

$$\begin{cases} rY_{14} = l[(l+1)\eta + 2\xi]r^{-(l-1)}, \\ r^2Y_{24} = 2\mu l[-(l+1)(l+2)\eta - 4\xi + 3]r^{-(l-1)}, \\ rY_{34} = [-l\eta + 2]r^{-(l-1)}, \\ r^2Y_{44} = 2\mu[l(l+2)\eta + 2l\xi - (2l+1)]r^{-(l-1)}, \\ Y_{54} = 4\pi G\rho l\xi r^{-(l-1)}, \\ rY_{64} = -4\pi G\rho l(l+1)\eta r^{-(l-1)}, \end{cases} \quad (8b)$$

whereas the fifth and sixth spheroidal solutions given by eqs (9) and (10) remain unchanged. The static spheroidal solutions eqs (4b), (5b), (7b) and (8b) are consistent with those derived by Pollitz (1992), but they are derived here in an independent way.

2.4 Degeneration caused by viscoelastic attenuation

Within the seismic band, the attenuation of seismic energy caused by the viscoelasticity is usually described through a constant quality factor for each of the P and S waves. Based on the correspondence principle, the viscoelastic dispersion and attenuation can be considered by introducing the complex wave velocities V_p and V_s (Kanamori & Anderson 1977; Müller 1983),

$$\begin{cases} V_p = V_p^o \left[1 + \frac{\ln(f/f_0)}{\pi Q_p} + \frac{i}{2Q_p} \right], \\ V_s = V_s^o \left[1 + \frac{\ln(f/f_0)}{\pi Q_s} + \frac{i}{2Q_s} \right], \end{cases} \quad (19)$$

where V_p^o and V_s^o are the P - and S -wave velocity at a reference frequency (e.g. 1 Hz), and Q_p and Q_s are the corresponding quality factors, respectively. Thus the arguments x_p and x_s take generally complex values, too.

In the case that $|\text{Im}(x)| \gg 1$, the spherical Bessel functions $j_l(x)$ and $y_l(x)$ can become linearly dependent even if l is not extremely large, implying that the degeneration problem can also be attributed to the viscoelastic attenuation. Consequently, the converging and diverging pairs of the fundamental solutions, that is eqs (1) and (2), (4) and (5) and (7) and (8), are no longer mutually independent. It seems that this problem can be avoided by using the spherical Hankel functions

$$\begin{cases} h_l^{(1)}(x) = j_l(x) + i y_l(x), \\ h_l^{(2)}(x) = j_l(x) - i y_l(x), \end{cases} \quad (20)$$

instead of the spherical Bessel functions $j_l(x)$ and $y_l(x)$, respectively. However, the same problem arises at the other end, that is when $|x| \rightarrow 0$. An optimal way is to replace only $y_l(x)$ in eqs (2), (5) and (8) by $h_n(x)$, where

$$h_l(x) = \begin{cases} h_l^{(1)}(x), & \text{if } \text{Im}(x) \geq 0, \\ h_l^{(2)}(x), & \text{if } \text{Im}(x) < 0. \end{cases} \quad (21)$$

According to the geophysical convention of forward and inverse Fourier transform, we need to use $h_l^{(2)}$.

Up to now, all fundamental solutions for seismic wave propagation in a spherical shell are given in the analytical form and the degeneration problems associated with them in the extreme cases are solved. Based on these results, a propagator algorithm for synthetic seismograms of a layered spherical Earth can be easily formulated in analogy to the reflectivity method for layered half-space models.

2.5 Haskell propagator for a layered viscoelastic sphere

If the displacement–stress vector is given by $\mathbf{y}(r_1)$ at one interface, say r_1 , its value $\mathbf{y}(r_2)$ at the next interface is related with $\mathbf{y}(r_1)$ through the Haskell propagator, defined by $\mathbf{H}(r_2, r_1)$,

$$\mathbf{y}(r_2) = \mathbf{H}(r_2, r_1) \mathbf{y}(r_1). \quad (22)$$

As an example, we derive the spherical Haskell propagator for the toroidal mode. In this case, $\mathbf{H}(r_2, r_1)$ can be expressed in the form,

$$\mathbf{H}(r_2, r_1) = \mathbf{A}(k_s r_2) \cdot \mathbf{A}^{-1}(k_s r_1), \quad (23)$$

where $\mathbf{A}(x)$ is a 2×2 matrix consisting of the fundamental solutions eqs (1) and (2) (after y_l is replaced by h_n) as the column vectors,

$$\mathbf{A}(x) = \begin{pmatrix} j_l(x) & h_l(x) \\ \mu [(l-1)j_l(x) - x j_{l+1}(x)] & \mu [(l-1)h_l(x) - x h_{l+1}(x)] \end{pmatrix}. \quad (24)$$

Theoretically both spherical Bessel and Hankel functions in eq. (24) can be easily calculated using their recursive relations. Practically, however, underflow and overflow can arise because $j_l(x)$ decreases and $h_l(x)$ increases exponentially with l when $l \gg |x|$. Fortunately, in the propagator algorithm we do not need the absolute but relative values of $j_l(x)$ and $h_l(x)$ within an arbitrary homogeneous spherical shell from r_1 to r_2 . For this reason, we normalize the left column of matrix $\mathbf{A}(x)$ by $[j_l(x) + ix j_{l+1}(x)]$ and the right-hand column by $h_l(x)$, and reformulate $\mathbf{H}(r_2, r_1)$ to

$$\mathbf{H}(r_2, r_1) = \mathbf{B}(k_s r_2) \cdot \mathbf{E}(k_s r_2, k_s r_1) \cdot \mathbf{B}^{-1}(k_s r_1), \quad (25)$$

where

$$\left\{ \begin{array}{l} \mathbf{B}(x) = \begin{pmatrix} 1 - z_l^{(j)}(x) & 1 \\ \mu \left[(l-1) \left[1 - z_l^{(j)}(x) \right] + iz_l^{(j)}(x) \right] & \mu \left[(l-1) - z_l^{(h)}(x) \right] \end{pmatrix}, \\ \mathbf{E}(x_2, x_1) = \begin{pmatrix} \exp \left[w_l^{(j)}(x_2, x_1) \right] & 0 \\ 0 & \exp \left[w_l^{(h)}(x_2, x_1) \right] \end{pmatrix}, \end{array} \right. \quad (26)$$

and $z_l^{(j)}(x)$, $z_l^{(h)}(x)$, $w_l^{(j)}(x_2, x_1)$ and $w_l^{(h)}(x_2, x_1)$ are new functions defined by

$$\left\{ \begin{array}{l} z_l^{(j)}(x) = \frac{ix j_{l+1}(x)}{j_l(x) + ix j_{l+1}(x)}, \\ w_l^{(j)}(x_2, x_1) = \ln \frac{j_l(x_2) + ix_2 j_{l+1}(x_2)}{j_l(x_1) + ix_1 j_{l+1}(x_1)}, \\ z_l^{(h)}(x) = \frac{x h_{l+1}(x)}{h_l(x)}, \\ w_l^{(h)}(x_2, x_1) = \ln \frac{h_l(x_2)}{h_l(x_1)}. \end{array} \right. \quad (27)$$

Note that the choice of the normalization factors $[j_l(x) + ix j_{l+1}(x)]$ and $h_l(x)$ is based on the criterion that they never become zero. The reformulated propagator eq. (25) is fully in analogy to the propagator in the case of a plane Earth model. The new functions defined in eq. (27) can be calculated using the following recursive relations:

$$\left\{ \begin{array}{l} z_l^{(j)}(x) = \frac{ix^2 \left[1 - z_{l+1}^{(j)}(x) \right]}{(2l+3+ix^2) \left[1 - z_{l+1}^{(j)}(x) \right] + iz_{l+1}^{(j)}(x)}, \\ w_l^{(j)}(x_2, x_1) = w_{l-1}^{(j)}(x_2, x_1) - \ln \frac{x_2}{x_1} + \ln \frac{x_2^2 + [1 - x_2^2 + i(2l+1)] z_{l-1}^{(j)}(x_2)}{x_1^2 + [1 - x_1^2 + i(2l+1)] z_{l-1}^{(j)}(x_1)} \\ z_l^{(h)}(x) = (2l+1) - \frac{x^2}{z_{l-1}^{(h)}(x)}, \\ w_l^{(h)}(x_2, x_1) = w_{l-1}^{(h)}(x_2, x_1) + \ln \frac{x_2}{x_1} + \ln \frac{2l+1 - z_l^{(h)}(x_2)}{2l+1 - z_l^{(h)}(x_1)}. \end{array} \right. \quad (28)$$

Note that all recursive formulae need to be performed upwards from smaller l to larger l , except for the function $z_l^{(j)}(x)$, which should be calculated recursively from larger l to smaller l . Otherwise, unstable results may arise (Takeuchi & Saito 1972).

The recursive calculation of $z_l^{(j)}(x)$ can start at a sufficiently large l , where an approximation based on eq. (11) can be used,

$$z_l^{(j)}(x) \sim \frac{x^2}{x^2 - (2l+3)i}, \quad \text{for } l \gg |x|. \quad (29)$$

For $l > |x_s|^2/2$, we design the toroidal propagator using the reformulated fundamental solutions eqs (1b) and (2b). In this case, the matrices $\mathbf{B}(x)$ and $\mathbf{E}(x_2, x_1)$ are replaced by

$$\left\{ \begin{array}{l} \mathbf{B}(x) = \begin{pmatrix} \phi_l(x) & \varphi_l(x) \\ \mu \left[(l-1) \phi_l(x) - \frac{x^2}{2l+3} \phi_{l+1}(x) \right] & \mu \left[(l-1) \varphi_l(x) - (2l+1) \varphi_{l+1}(x) \right] \end{pmatrix}, \\ \mathbf{E}(x_2, x_1) = \begin{pmatrix} \left(\frac{r_2}{r_1} \right)^l & 0 \\ 0 & \left(\frac{r_2}{r_1} \right)^{-(l+1)} \end{pmatrix}. \end{array} \right. \quad (30)$$

The Haskell propagator associated with the spheroidal solutions can be derived in a similar way. These spherical propagators that we show here for the first time have the same form like those used for a plane Earth model. Therefore, all established methods for numerical efficiency and stability of the half-space propagator algorithm can be adopted simply for the spherical geometry.

3 ALGORITHM

In our hybrid algorithm, a critical frequency f_o (~ 0.03 Hz) and a critical harmonic degree l_o (~ 300) are defined for calculating the spheroidal modes. For $f \leq f_o$ and $l \leq l_o$, the gravity effect is accounted for and the solutions are obtained through the Runge–Kutta integration of the

equations described in the Appendix. When $f > f_o$ or $l > l_o$, the gravity effect is neglected and the Haskell propagator algorithm is used. Note that the numerical solutions always differ from the analytical ones. Though such differences might be very small, they may cause a visible non-physical phase traveling with an apparent velocity determined by f_o and l_o . To avoid this artefact, we suggest the use of a certain transition band around f_o and l_o , in which both numerical and analytical results are calculated and then combined linearly to ensure a smooth continuity at $f = f_o$ and $l = l_o$. Based on our tests, the artefact can be effectively suppressed by using a transition band around f and l of about 20 per cent of f_o and l_o , respectively.

The computation procedure can be designed with two loops over the spherical harmonic degree l and the frequency f . Since the frequency f is continuous, the time-domain aliasing problem may be caused by discrete sampling. In comparison, the harmonic degree l is inherently discrete. However, the space-domain aliasing problem can still be generated by cutting off at the harmonic degree l , especially if the observation sites are located at the same depth as the source. In addition, the loss-of-precision is well known, which can arise in results obtained from either the Runge–Kutta integration or the Haskell propagator. In the following two subsections, we introduce the methods useful for overcoming the loss-of-precision problem and suppressing the aliasing phases in synthetic seismograms.

3.1 The loss-of-precision problem

According to previous studies, the loss-of-precision problem can be avoided using either the reflectivity method (Fuchs & Müller 1971; Kennett 1983) or the second-order minor method (Knopoff 1964; Dunkin 1965; Gilbert & Backus 1966; Kind 1983; Friederich & Dalkomo 1995) or the orthonormal propagator method (Wang 1999; Wang & Kümpel 2003). Ma *et al.* (2012) have shown that all these three major methods are based on the same mathematical principle and therefore can solve the numerical problems equally well. In comparison, however, the orthonormal propagator method is the simplest for the implementation and the most efficient for the numerical computation. Therefore, we adopt the orthonormal propagator method in this study.

3.2 The time-domain aliasing problem

Theoretically, the time-domain aliasing problem does not exist if the normal mode method is used. In principle, seismograms can be expanded in terms of the fundamental spheroidal and toroidal modes and their overtones, that is the free oscillation spectra. Each fundamental mode or its overtone is represented by a pole in the Laplace plane. The normal mode method is used to locate the poles and characterize them for the amplitude, phase, frequency and quality factor. The normal-mode method is only efficient for synthetic seismograms at very low frequencies (≤ 0.15 Hz). At higher frequencies, the poles become closer to each other leading to inefficiency of their location and instability of their characterization. Consequently, the convergence is slower and the result is less accurate. Therefore, for complete seismograms at higher frequencies (e.g. up to 1–2 Hz) the discrete Fourier transform is more efficient than the normal-mode method.

The time-domain aliasing problem is inherent with the discrete frequency method. If an insufficient frequency sampling rate $\Delta f = 1/T$ is used, where T is the length of time window, all seismic phases with the real arrival time beyond the time window will appear in the beginning of the time window. Bouchon (1979) showed that the time-domain aliasing can be effectively suppressed by using the complex frequency technique. In fact, instead of the Fourier spectrum of a seismogram, say $Y(i\omega)$, the Laplace spectrum $Y(\sigma + i\omega)$ can be calculated with the same effort, where σ is a positive constant. The time-domain seismogram $y(t)$ is then obtained through the Riemann–Mellin integral,

$$y(t) = e^{\sigma t} \int_{-\infty}^{+\infty} Y(\sigma + i\omega) e^{i\omega t} df = e^{\sigma t} \mathcal{F}^{-1}[Y(\sigma + i\omega)], \quad (31)$$

where \mathcal{F}^{-1} represents the inverse Fourier transform. Note that $Y(\sigma + i\omega)$ is the Fourier spectrum of the function $e^{-\sigma t}y(t)$. If the discrete Fourier transform, for example, fast Fourier transform (FFT), is applied to eq. (31), the time-domain aliasing phases can be suppressed by factor $e^{-\sigma T}$. However, the expense for this anti-aliasing technique is a minor loss of the signal-to-noise ratio at the end of the time window depending on the value chosen for σ . An example is shown in the electronic supplement material to demonstrate how the time-domain aliasing can be suppressed using the complex frequency method (Fig. S1).

3.3 The space-domain aliasing problem

The space-domain aliasing appears especially if the observation sites are located at a depth equal or very close to that of the source. In such a case, the spherical harmonic spectra of seismograms are dominated by the near-field terms, which are smooth and converge slowly to zero or are constant with the harmonic degree. The content of regional and teleseismic signals is represented by a small oscillatory part superposed on the large smooth basis. Consequently, any cut-off of the spherical harmonic degree affects the spectral information strongly and results in non-physical wave phases in synthetic seismograms.

The space-domain aliasing can be suppressed in a similar way as for the time-domain aliasing. Assume that

$$y(\theta) = \sum_{l=m}^{\infty} F_l P_l^m(\cos \theta), \quad (m \geq 0), \quad (32)$$

where θ is the angular epicentral distance, and $P_l^m(x)$ are the associated Legendre polynomials of degree l and order m . Wang & Wang (2007) showed that the function $y(\theta)$ can be expressed equivalently by

$$y(\theta) = \frac{1}{2\sin^2(\frac{\theta}{2})} \sum_{l=m}^{\infty} G_l P_l^m(\cos\theta), \quad (m \geq 0), \quad (33)$$

where G_l represents the Legendre spectrum of the function $2\sin^2(\theta/2) \cdot y(\theta)$ and is related to F_l by

$$G_l = \begin{cases} F_l - \frac{l+m+1}{2l+3} F_{l+1}, & l = m, \\ F_l - \frac{l+m+1}{2l+3} F_{l+1} - \frac{l-m}{2l-3} F_{l-1}, & l > m. \end{cases} \quad (34)$$

Note that for large l , $G_l \sim F_l - (F_{l+1} + F_{l-1})/2 = -\Delta^2 F_l/2$, where Δ^2 represents the second-order finite difference operator. Therefore, eq. (34) is called the differential transform (Wang & Wang 2007). For observation sites in the far field, the necessary cut-off harmonic degree for calculating $y(\theta)$ can be considerably reduced by using eq. (33) instead of (32). As shown in Wang & Wang (2007), sometimes it is even necessary to use a higher-order differential transform depending on where and how sharp the user wants to cut off the harmonic spectrum. An application example of the differential transform is shown in the electronic supplement material (Figs S2 and S3).

3.4 Implementation of the code QSSP

In our QSSP code, a large earthquake is represented by a number of point sources and synthetic seismograms are calculated in two steps. First, for a given depth level of seismic stations, a database of spectral Green's functions for discrete source depths is created, which can then be used repeatedly to synthesize seismograms for any earthquake described with a finite-fault kinematic source model. With personal PCs nowadays, the maximum harmonic degree can be defined as large as 25 000. If the complete waveform is desired, the frequency range can cover from 0 to 2 Hz or higher at the global scale. The discrete point sources can be represented as double-couples or as full moment tensors. They can be placed in any layer in the solid Earth, but also in the oceanic or atmospheric layers. Earth models used can include optionally the solid inner core, the liquid outer core, the mantle, the ocean and the atmosphere, each of which can have a multilayered structure. All computations are carried out using a single code and controlled with a self-explanatory input file.

4 TESTS

In this section, we show several computation tests of the QSSP code. In Test 1, teleseismic synthetic seismograms are calculated and compared with those obtained by the reflectivity code, revealing the Earth curvature effect. Test 2 demonstrates the gravity effect on long-period Rayleigh waves and free oscillations. In Test 3, tsunami and infrasound waves excited by the 2004 M_w 9.3 Sumatra earthquake are simulated. Test 4 shows a near-field displacement seismogram with static offset calculated for the 2011 M_w 8.8 Maule earthquake in comparison with the high-rate GPS data. Finally, Test 5 shows a cross check between QSSP and the code PSGRN/PSCMP (Wang *et al.* 2006) for a static dislocation model. Additional examples are provided in the electronic supplement material.

4.1 The Earth curvature effect at teleseismic distances—comparison with the reflectivity code

So far complete synthetic seismograms are computed by the widely used reflectivity code based on a layered half-space model, in which the Earth curvature effect is considered approximately through an earth-flattening transformation (EFT) developed by Müller (1977). Using the EFT, body waves observed at the surface of a spherical model can be simulated using a properly stratified half-space model. The EFT formulae were validated originally only for a homogeneous sphere. It is interesting to see how well the EFT works for a realistic Earth model. For this purpose, we use the seismic reference model AK135 (Kennett *et al.* 1995) and compare complete synthetic seismograms for very large distances calculated by the reflectivity code QSEIS implemented based on Wang (1999) and the code QSSP developed in this study, respectively. Velocity seismograms are calculated for an explosion source in 230 km depth and for arrivals before the pS phase (Fig. 1). At distances within about 140°, most body waves based on the two models agree with each other not only for the arrival time but also for the waveform and amplitude. Large differences are found for surface waves and few complicated multiple waves as well. In particular, the EFT fails for distances close to 180° and waves that exist only due to the spherical geometry, such as for example, the P'P' (PKPPKP) phase, cannot be produced using a plane Earth model. The arrivals of multipathing rays through the outer and inner core lead to significant high-frequency energy at large epicentral distances and late times (e.g. >1200s at 120°), which are not modelled by flat-earth reflectivity codes. Therefore, QSSP has a potential for improving studies on the structure and attenuation of the outer and inner core from multiple pathing body (e.g. Ivan & Wang 2013) and surface waves. Note that the results shown in Fig. 1 also provide a cross validation between the two independent codes QSEIS (Wang 1999) and QSSP. More examples for calculating multiple core phases like PmKP ($m \leq 10$) are shown in the electronic supplement material (Figs S4–S7).

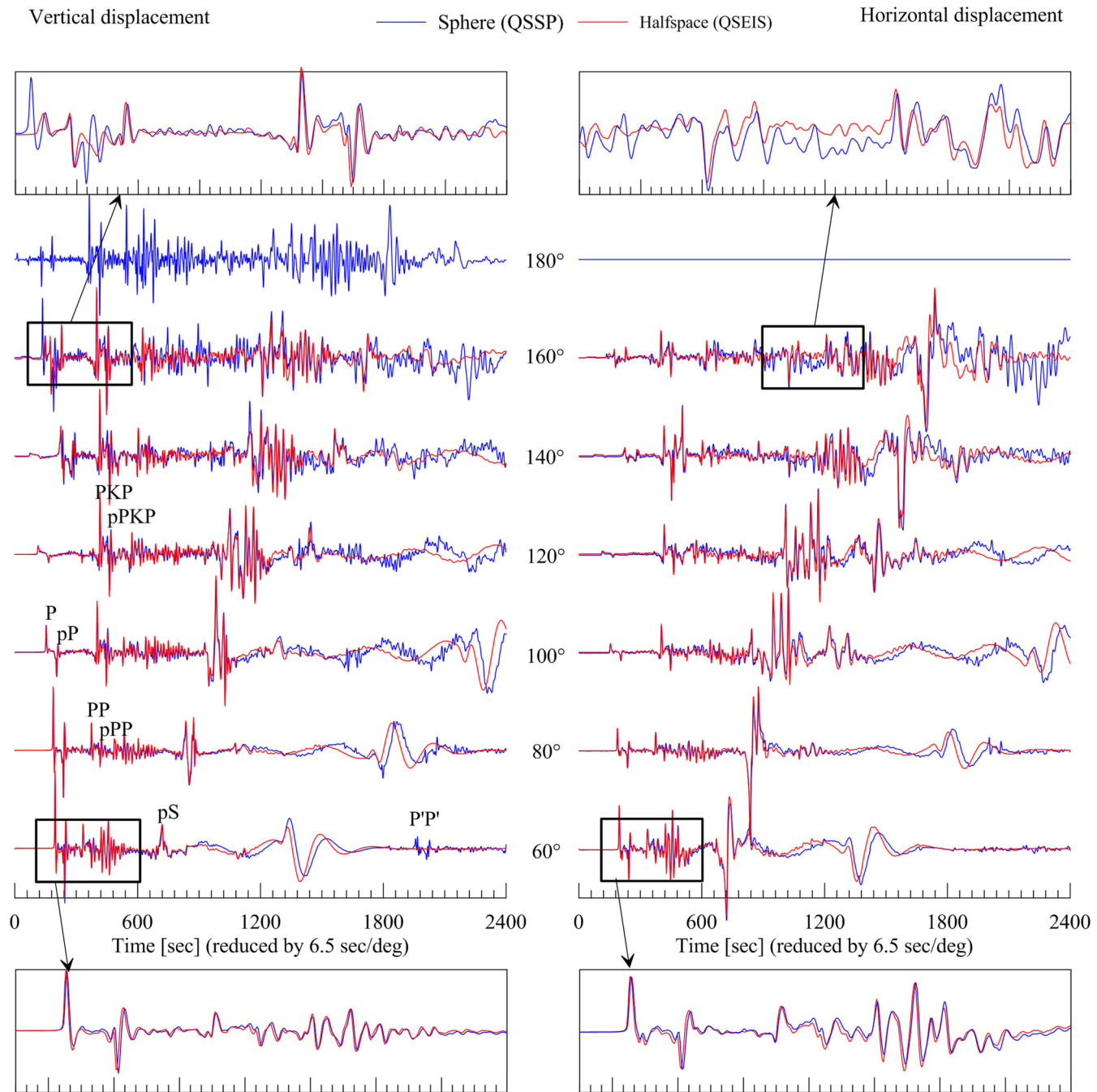


Figure 1. Comparison of teleseismic (60° – 180°) synthetic seismograms computed using the QSSP code (this study) based on the spherical Earth model AK135 and the QSEIS code (Wang 1999) based on the corresponding plane-earth model with the earth-flattening transformation. A point explosion source at the depth of 210 km is used. The cut-off frequency is 1.0 Hz. The four zoomed windows are selected to show the agreements or disagreements between the results from two different codes more clearly.

4.2 The gravity effect on long-period Rayleigh waves and free oscillations

In this test a long time window of 12 hr is chosen to include Rayleigh waves circling several times around the Earth. Fig. 2 shows synthetic seismograms of the vertical component at the distance of 90° for a strike-slip source at the depth of 33 km. To demonstrate the gravity effect, the synthetics are calculated by switching on and off the gravity-deformation coupling in the hybrid algorithm, that is by selecting $f_o/l_o = 0.03 \text{ Hz}/300$ and $0.0 \text{ Hz}/0$, respectively. As expected, the gravity effect is significant only for very long-period Rayleigh waves and late arriving global Rayleigh wave groups. At periods of a few minutes or longer, the Earth gravity may delay the arrival time by about a half period and modify the waveform considerably. Analysis of such wave trains, as for example the moment tensor inversion from long period surface waves for mega-thrust earthquakes, may be biased if the gravity effect is not properly considered. Note that gravity can also affect the

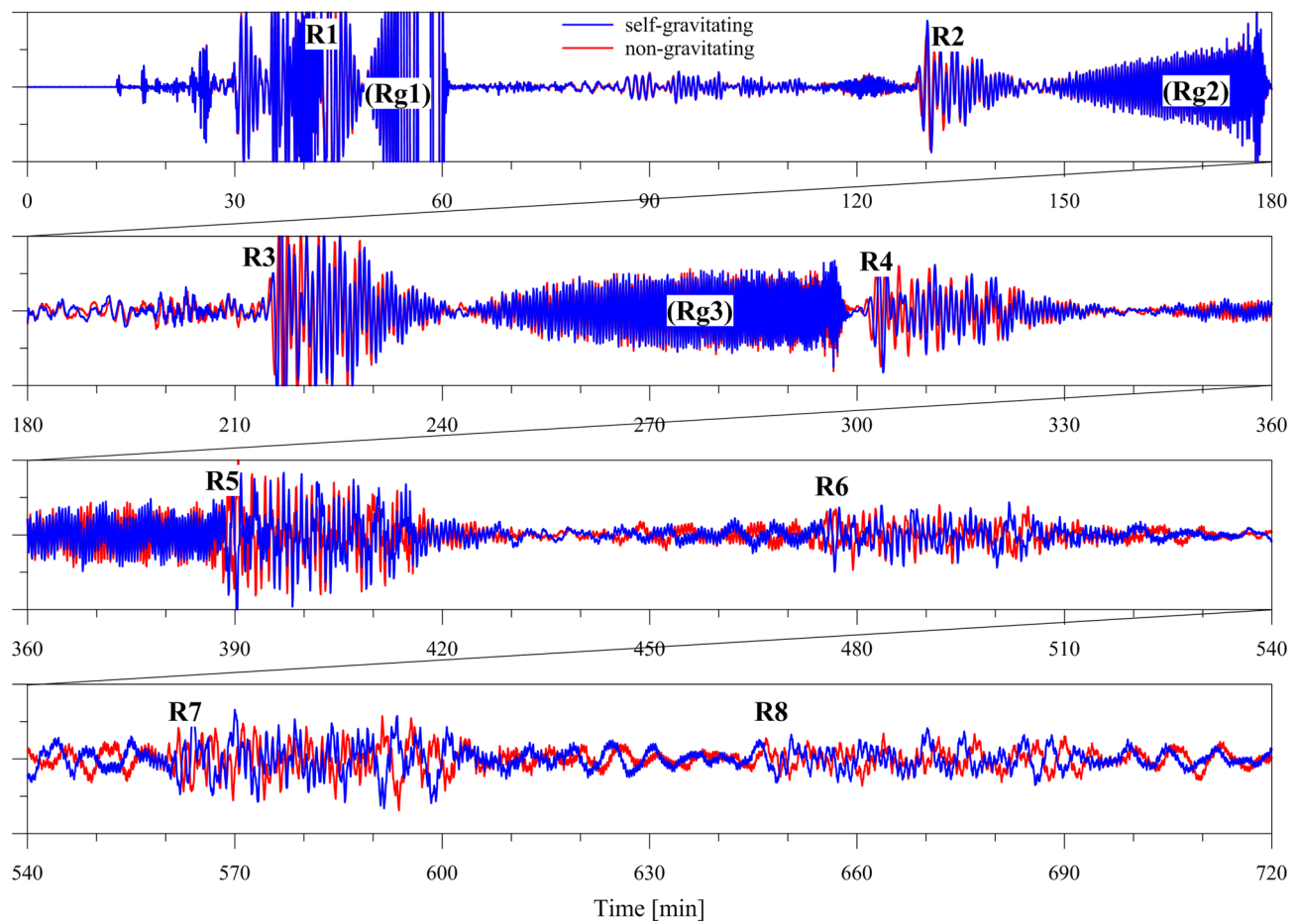


Figure 2. Comparison of synthetic broad-band seismograms (vertical component) calculated based on the Earth model AK135 with and without the gravity effect. The source is an impulsive strike-slip double-couple at the depth of 33 km, and the observation site is located at the epicentral distance of 90°. The whole time window is 12 hr and is divided into four equal subwindows, each being scaled individually. The cut-off frequency is 0.1 Hz. R1–8 denote the global Rayleigh wave groups.

W-phase leaky mode, which is nowadays used for fast moment tensor inversion, although the effect is much smaller there (see Fig. S8 in the electronic supplement material).

Next we calculate the free oscillation spectra caused by the 2004 M_w 9.3 Sumatra earthquake. For simplicity, the earthquake source is simplified by a point thrust (dip = 8°) dislocation at the depth of 30 km. Fig. 3 shows the Fourier amplitude spectra of the spherical harmonic terms of degree 0, 1 and 2. The spheroidal and toroidal modes are denoted by ${}_nS_l$ and ${}_nT_l$, respectively. Their fundamental frequencies ($n = 0$) and overtones ($n \geq 1$) are clearly identified by the amplitude peaks. Note that the toroidal modes ${}_nT_0$ are meaningless per definition. The fundamental modes ${}_0S_1$ and ${}_0T_1$ are missing because they would mean a translational motion of the mass centre of the Earth and a rigid rotation of the Earth, respectively, which can never be excited by any internal force like earthquakes. The gravity effect on ${}_0S_0$ is the most significant, causing a decrease of the frequency by 0.1249 mHz or 13.30 per cent.

The spheroidal mode ${}_1S_1$ is characterized by the translational oscillation of the inner solid core. Because of the Earth's rotation and elliptical figure, there exist the axial, prograde and retrograde modes of ${}_1S_1$, which are known as the Slichter triplet (Slichter 1961). The splitting is dominantly caused by the Coriolis force due to the Earth's rotation (Dahlen 1968; Dahlen & Tromp 1998). In particular, the retrograde mode has the largest frequency (shortest period) of the triplet because the Coriolis force enhances the elasto-gravitational feedback, and vice versa for the prograde mode. It is known that the frequency of the Slichter mode is strongly dependent on the density contrast between the inner and outer core. The smaller the density contrast, the longer the period. Therefore, the observation of the Slichter mode would provide a useful constraint on the inner and outer core structure. So far, there have been many claims of observation of the Slichter triplet mostly based on the records of superconducting gravimeters, good evidence is still lacking (see e.g. Hinderer *et al.*, 1995; Ochi *et al.* 2000; Rosat *et al.* 2006; Ding & Chao 2015).

Fig. 4 shows the power spectrum around ${}_1S_1$, whose degenerate frequency (period) and Q value are determined at 51.1824 μHz (5.4272 hr) and 6060 for the PREM model (Dziewonski & Anderson 1981), respectively. The very large Q value results from the nearly inviscid fluid outer core used in the model. Our estimate of the degenerate period agrees well with the recent results (5.219–5.420 hr) obtained by different authors based on the same Earth model PREM (Crossley 1993; Rochester & Peng 1993; Peng 1997; Rogister 2003), but it is significantly larger than those (4.309–4.600 hr) based on the earth model 1066A (Dahlen & Sailor 1979; Crossley *et al.* 1992; Crossley 1993;

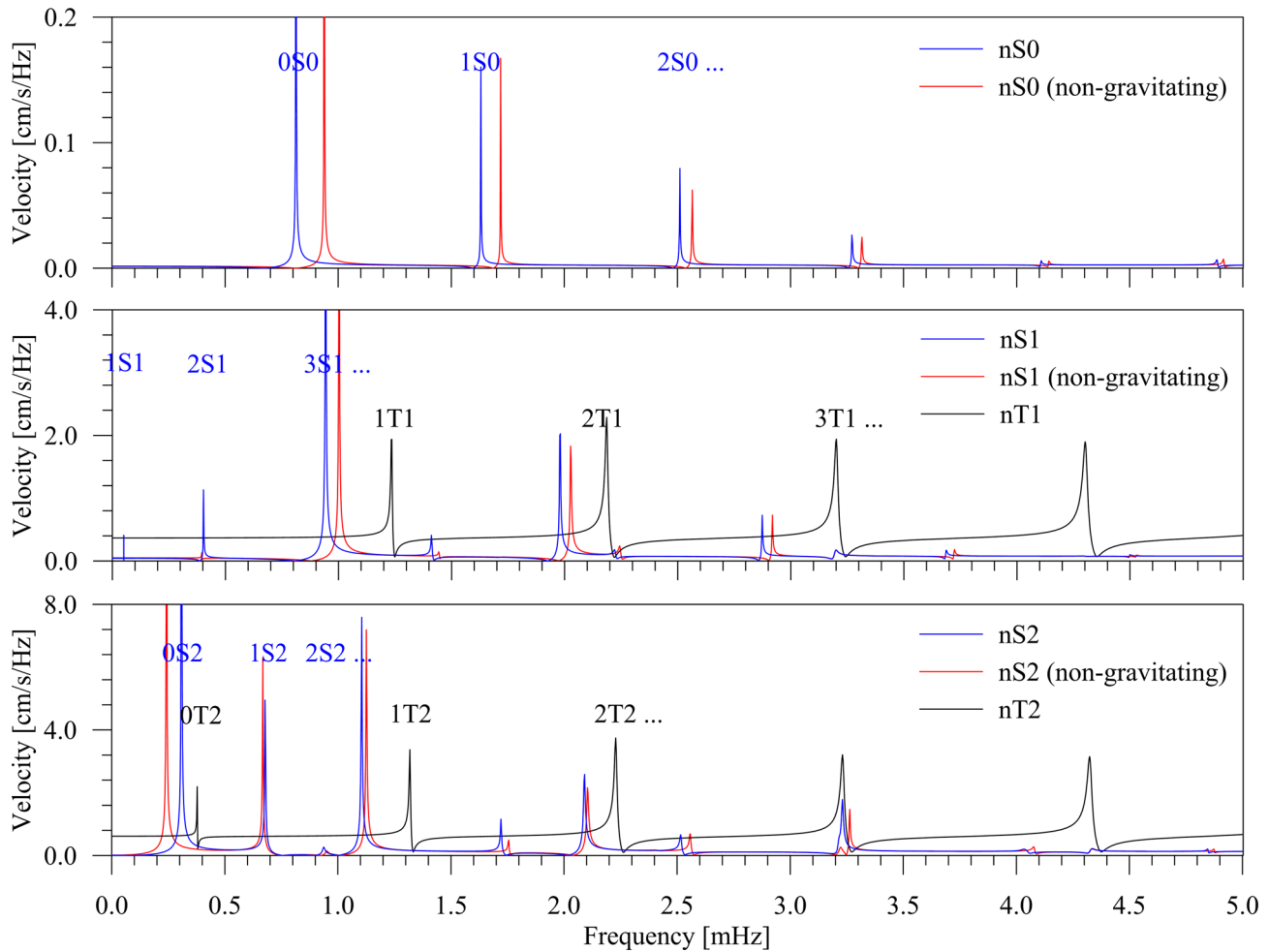


Figure 3. Comparison of the Fourier amplitude spectra of free oscillations (${}_n S_l$ and ${}_n T_l$ for ≤ 2) calculated based on the Earth model PREM with and without the gravity effect. The source is adopted from Harvard's CMT double-couple for the 2004 M_w 9.3 Sumatra earthquake, and the observables are the surface velocity as measured by a broad-band seismometer located at the epicentre. Note that the resonance peaks become asymmetric if the background spectral level contributed from the neighbouring modes is significant.

Rieutord 2002; Rogister 2003). The peak displacement amplitude of ${}_1 S_1$ caused by the 2004 M_w 9.3 Sumatra earthquake are estimated to be $0.27 \mu\text{m}$ on the surface and 0.29 mm in the inner core if the earthquake source is simplified by a point dislocation ($M_w = 9.3$, strike = 329° , dip = 8° , rake = 110° , latitude = 3.09° , longitude = 94.26° and depth = 30 km). Correspondingly, the maximum gravity change on the surface is in the order of 0.1 nGal (including both inertial and free-air effects, as could be measured by a gravimeter). If the finite-fault source model derived from the near-field GPS data (Hoechner *et al.* 2008) is used, however, the amplitudes of the three observables are increased to $0.79 \mu\text{m}$, 0.83 mm and 0.25 nGal , respectively. Note that the free-air gradient of the surface gravity is $0.30827 \text{ nGal } \mu\text{m}^{-1}$. Therefore, the 0.25 nGal gravity change results almost from the free-air effect. The inertial part and the part due to the mass redistribution are together only about 0.5 per cent of the free-air effect, that is 1.25 nGal , for the Slichter mode.

If the rotational and elliptical splitting is considered, the Slichter triplet frequencies of the PREM model can be derived from its degenerate frequency based on the perturbation theory. Using the formulae by Dahlen (1968) and Dahlen & Sailor (1979), which include a slight shift in addition to the splitting, we obtain $51.918 \mu\text{Hz}$ (5.350 hr), $45.948 \mu\text{Hz}$ (6.045 hr) and $57.831 \mu\text{Hz}$ (4.803 hr) for the axial, prograde and retrograde modes, respectively. Correspondingly, the global gravity change caused by the Slichter triplet, as it could be measured by gravimeters on the Earth's surface, can be expressed in the form

$$\Delta g(\theta, \varphi, t) = A_a \cos(\theta) \cos(\omega_a t + \delta_a) + \sin(\theta) [A_p \cos(\omega_p t - \varphi + \delta_p) + A_r \cos(\omega_r t + \varphi + \delta_r)], \quad (35)$$

where θ is the colatitude, φ is the longitude, the indices (a, p, r) denote the axial, prograde and retrograde modes, and (A, ω, δ) are their amplitude, frequency and initial phase, respectively. We may assume that the amplitudes and initial phases of the Slichter triplet are not significantly influenced by the Earth's rotation like their frequencies. By calculating the frequency-domain resonance responses (before the inverse Fourier transform) at three different locations on the Earth's surface, we are able to estimate the amplitudes and phases of the Slichter triplet excited by the 2004 great Sumatra earthquake without taking into account for the effect of the Earth's rotation. Using the finite-fault source and the PREM model, we obtain that $(A_a, \delta_a) = (0.032 \text{ nGal}, 175^\circ)$, $(A_p, \delta_p) = (0.125 \text{ nGal}, 269^\circ)$ and $(A_r, \delta_r) = (0.125 \text{ nGal}, 83^\circ)$. These results indicate that in the present case the Slichter mode is dominated by the motion within the equatorial plane

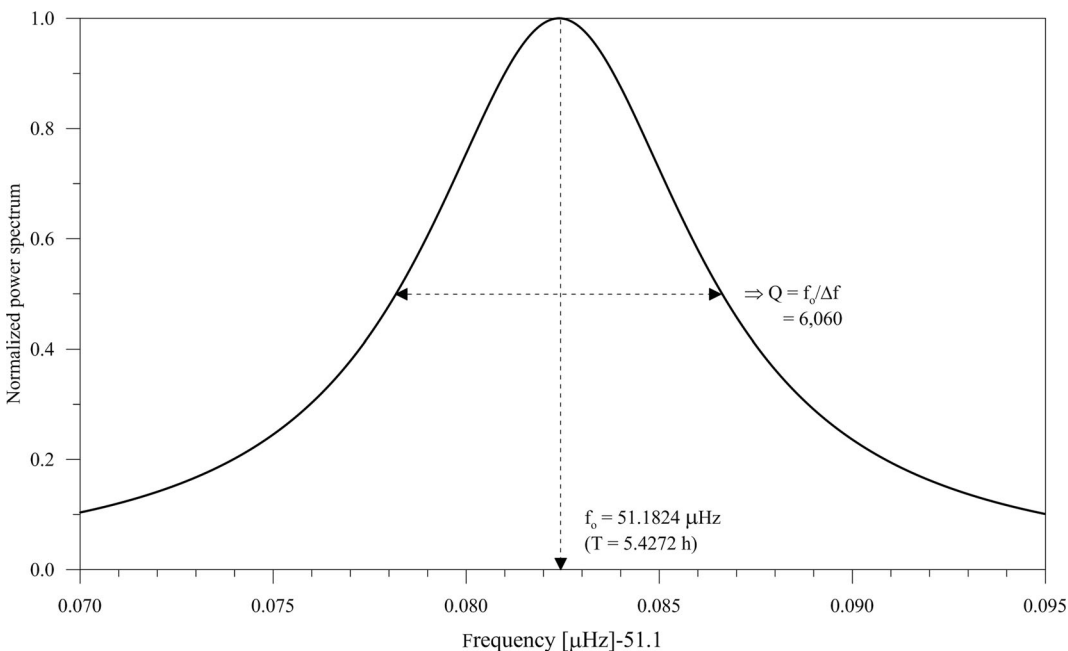


Figure 4. Fourier power spectrum around the spheroidal mode ${}_1S_1$ (Slichter mode) calculated using the Earth model PREM. The source is adopted from Harvard's CMT double-couple solution for the 2004 M_w 9.3 Sumatra earthquake at the depth of 30 km, and the observable is the vertical ocean-bottom velocity at the epicentre.

because of the near-equator location of the exciting source. Furthermore, the equal amplitude of the prograde and retrograde modes means that the inner core oscillates in principle like a Foucault pendulum. However, in contrast to the Foucault pendulum the prograde and retrograde Slichter singlets are also influenced by the elasticity of the Earth (particularly of the outer core). The splitting is therefore not only defined by the Coriolis force but also by the elastic forces. The induced gravity change starts with its negative peak value of about -0.25 nGal in the epicentral area and positive peak value of $+0.25$ nGal at the antipodal area of the earthquake. The peak to peak amplitude around the equator in the post-seismic period may reach about 0.5 nGal, which is more than twice as large as that estimated using the point source approximation, but still orders of magnitude smaller than what can be resolved by a modern superconducting gravimeter, explaining how challenging would be the observations of the Slichter modes if they are excited seismically.

Complete normal modes in the low frequency band of up to 2.0 mHz are shown in the electronic supplement material (Table S1). For the same Earth model (the isotropic version of PREM), the eigenfrequencies calculated by QSSP agree excellently with those by MINEOS (<0.04 per cent), but the Q values given by QSSP are systematically smaller than those by MINEOS (maximum of 11 per cent for ${}_0S_0$). We explain the large discrepancy in the Q values by the approximation approach used in MINEOS to determine the attenuation effect. Actually, MINEOS calculates the normal modes in two steps. First the eigenfrequency and eigenfunction are determined for a purely elastic Earth model without attenuation. Then the quality factor (equivalent to the imaginary part of eigenfrequency) and its effect on the eigenfrequency are estimated using the first-order perturbation method. In contrast, QSSP determines the eigenfrequency and quality factor simultaneously using the correspondence principle without any approximation.

4.3 Tsunami and infrasound waves

In this test, synthetic seismograms for tsunami and infrasound waves caused by the 2004 M_w 9.3 Sumatra earthquake are computed with the code QSSP. The Earth model used is the PREM model, which includes 3 km ocean layer, combined with a standard atmosphere up to 86 km height (U.S. Standard Atmosphere: U.S. Government Printing Office, Washington, DC, 1976). We calculate the pressure changes along a southward profile from the epicentral distance of 10° to 70° using a realistic earthquake source model, which consists of 432 subfaults with the slip distribution adopted from Hoechner *et al.* (2008). The results are shown in Fig. 5. At the ocean bottom, Rayleigh waves and tsunami waves are visible. The latter propagate with a velocity of about 170 m s $^{-1}$, consistent with the ocean depth of 3 km. At the ocean surface, acoustic-infrasound gravity waves are visible additionally, which propagate through the atmosphere with the velocity smaller than 340 m s $^{-1}$ (the near-ground sound speed). The acoustic-infrasound waves are missing (insignificant) at the ocean bottom because of the isostatic equilibrium. It is interesting to see that the tsunami wave can cause the pressure changes not only at the ocean bottom but also at the ocean surface and the tsunami waveforms observed at the two different levels have the opposite polarization. The reason is that for any water level change of Δh , the pressure change is $\rho_w g \Delta h$ if it is measured by a sensor fixed at the ocean bottom, but $-\rho_a g \Delta h$ if it is measured by a sensor swimming on the water surface, where ρ_w and ρ_a are the densities of water and air, respectively. The complicated infrasound and tsunami waveforms shown in Fig. 5 are not only related to the near-field ocean bottom motion calculated using the kinematic finite-fault source model, which extends about 1000 km and lasted about 10 minutes, but also to the reverberation effect within the ocean layer.

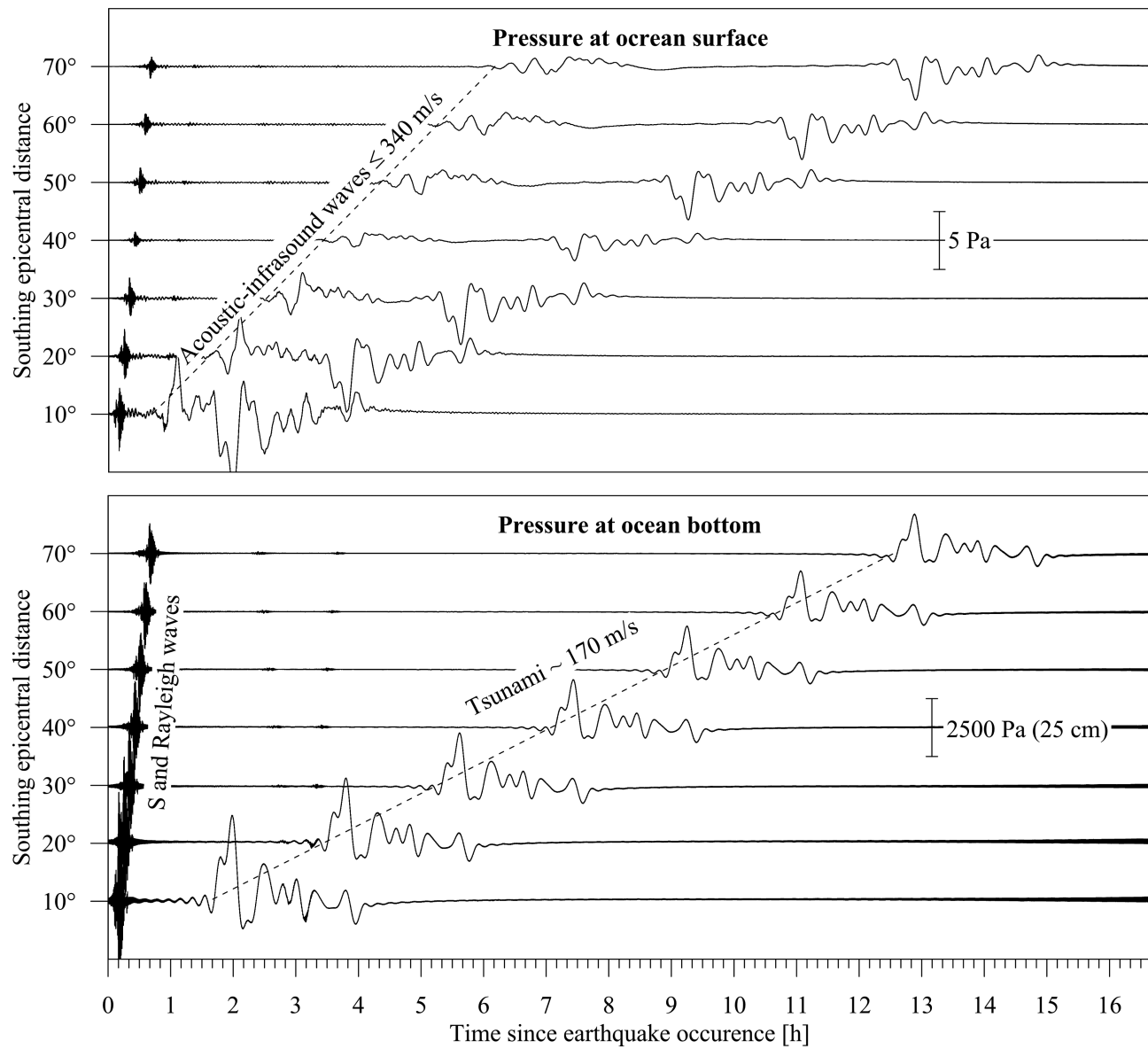


Figure 5. Synthetic seismograms for tsunami and infrasound waves caused by the 2004 M_w 9.3 Sumatra earthquake. The Earth model used is PREM (with a uniform ocean layer of 3 km) combined with the standard U.S. atmosphere model, the earthquake source consists of 432 subfaults with the slip distribution adopted from Hoechner *et al.* (2008), the cut-off frequency is 0.04 Hz, and the receiver profile is southward from the earthquake epicentre.

Like the solid Earth, the atmosphere and the ocean can exhibit their own free oscillations, which are made through interference of infrasound and tsunami waves cycling around the Earth, respectively. Using the normal mode method, Lognonné *et al.* (1998) investigated the coupling between the solid Earth and atmosphere but without a global ocean. For convenience, we denote the atmospheric free oscillation modes by ${}_n A_l$ and the oceanic ones by ${}_n W_l$, in analogy to ${}_n S_l$ or ${}_n T_l$ for the solid Earth free oscillations. To study ${}_n A_l$, we combine the U.S. Standard Atmosphere model with a modified Earth model PREM (with 3 km frozen ocean) and calculate the Fourier spectra of synthetic infrasound seismograms. The results are shown in the upper panel of Fig. 6, where the long-period fundamental modes ${}_0 A_l$ for $l > 0$ are clearly identified by the Fourier amplitude peaks. The longest atmospheric free oscillation period is given by ${}_0 A_1$, which is estimated to be 27.4 hr for the U.S. standard model. ${}_0 A_0$ and ${}_n A_l$ for $n > 0$ are beyond the plotted frequency band. Similarly, the long-period fundamental modes ${}_0 W_l$ for $l > 0$ are shown in the lower panel of Fig. 6, which are calculated based on the original PREM with 3 km ocean layer. The longest oceanic free oscillation period belongs to ${}_0 W_1$ and is 52.8 hr for the PREM model.

Modelling and source inversion studies, which aim to combine seismic and oceanic layer pressure recordings, can benefit from an all-in-one code like QSSP which considers the full coupling of these waves. For instance, QSSP was used by Heimann *et al.* (2013) to estimate the source parameters of the 2013 Cheliabinsk meteorite explosion from seismic, long period Rayleigh waves, and by Raveloson *et al.* (2012) for interpreting the tsunami and acoustic-gravity signals of the 2004 Indian Ocean tsunami recorded by the IMS infrasound arrays.

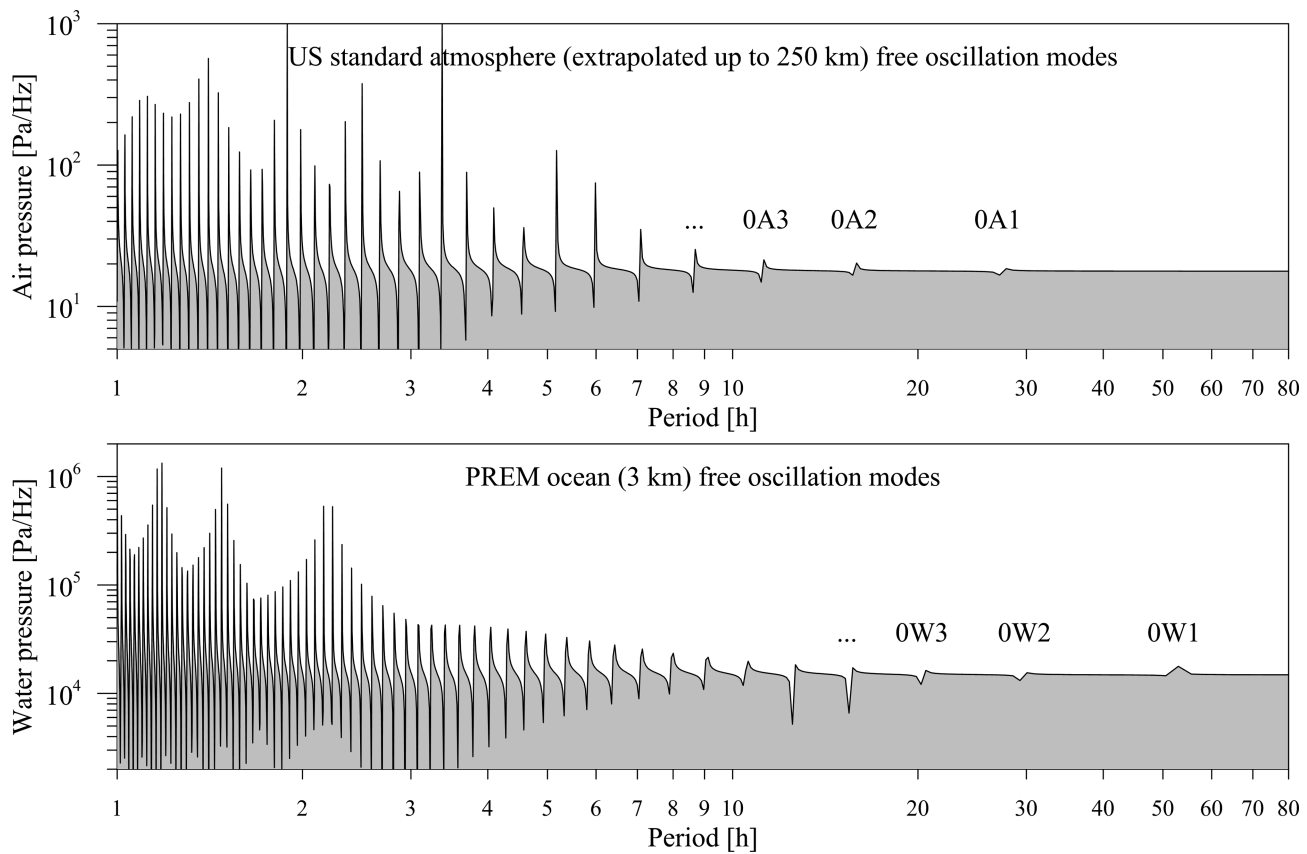


Figure 6. Long-period free oscillation modes of the atmosphere and ocean calculated using (1) the U.S. standard atmosphere (extrapolated up to 250 km) combined with the solid Earth model PREM and (2) the PREM model (with 3 km ocean), respectively. The spectra are modulated by the amplitude estimated for the 2004 M_w 9.3 Sumatra earthquake.

4.4 Near-field displacement seismograms with permanent offset

This test demonstrates the complete synthetic seismograms for the near-field displacement. As an example, the 2010 M_w 8.8 Maule (Chile) earthquake is considered. The fault slip model is adopted from Tong *et al.* (2010), derived from the InSAR and GPS data. This source model includes 1338 subfaults of the uniform size of 10 km. For simplicity, the kinematic rupture process is simulated using a uniform rupture propagation velocity of 2.65 km s^{-1} and the Brune's source time function with a uniform characteristic rise time of 1.5 s. Fig. 7 shows the synthetic displacement seismograms at Station ROBL ($-32.9760^\circ\text{N}, -71.0157^\circ\text{E}$), compared with the high-rate (1 sps) GPS data (Christophe Vigny, personal communication, 2011).

Note that there is a significant discrepancy between the vertical static offsets of the high-rate GPS data and the daily GPS data. As expected, the synthetic static offsets agree better with the daily GPS data, based on which the slip model was derived. The displacement time histories are not well reproduced like the static offsets, possibly because of the use of the simplified rupture-time and rise-time distributions, but also the neglecting of the non-global ocean effect. A possible contribution of QSSP is seen for the simultaneous inversion of high rate continuous GPS together with near field accelerometer and regional broad-band seismic data, for example to estimate the time dependent slip distribution of earthquakes. The advantage of QSSP is that all modelled Green's functions are based on the same method and the same Earth model parametrization.

4.5 Static deformation field and gravity changes near the earthquake fault

Here we demonstrate a cross check between QSSP and PSGRN/PSCMP (Wang *et al.* 2006) for calculating near-field static deformation and gravity changes caused by the 2007 M_w 7.7 Tocopilla (Chile) earthquake. A finite-fault source model is used, which consists of about 1000 fault patches adopted from Motagh *et al.* (2010). Comparisons of the 3-component surface displacement and gravity changes calculated using QSSP and PSGRN/PSCMP are shown in Figs 8 and 9, respectively. The differences between the results from the two independent codes are on the level of a few percent that is about within the expected numerical accuracy. It should be noted that PSGRN/PSCMP is based on a half-space geometry and the gravity effect is accounted for using the so-called Wang approach (Segall 2010). The good agreements shown in Figs 8 and 9 validate each other's performances of the two independent tools. Thus, QSSP can be beneficial for a joint inversion of InSAR derived static near-field displacements with teleseismic broad-band seismograms using a consistent method and Earth model parametrization.

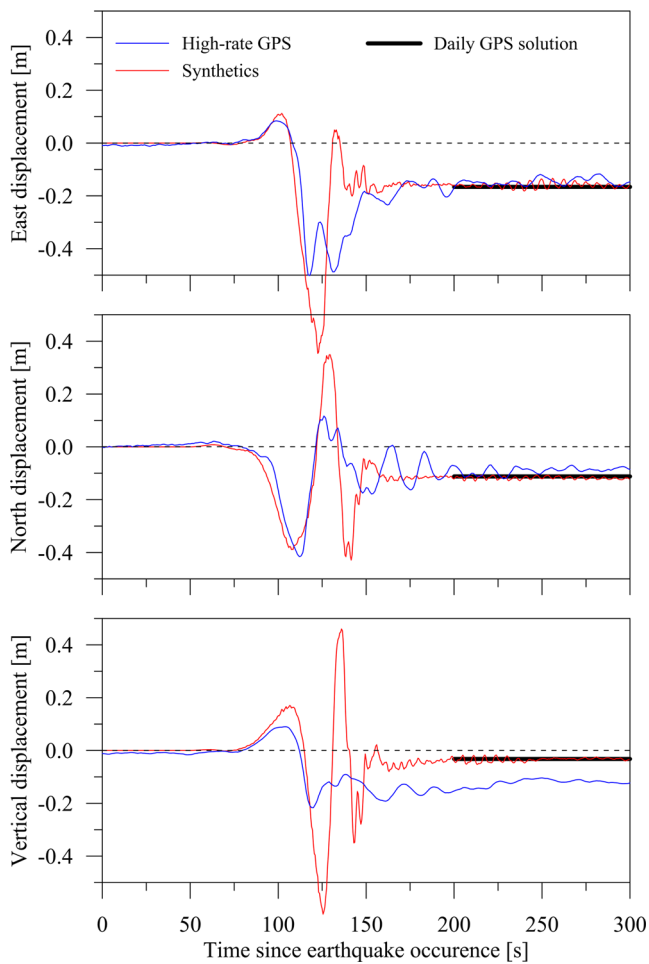


Figure 7. Comparison between the high-rate GPS and synthetic displacement seismograms at Station ROBL (-32.9760°N , -71.0157°E) for the 2010 M_w 8.8 Maule (Chile) earthquake. The earthquake source used is the finite-fault model adopted from Tong *et al.* (2010).

Additionally, QSSP helps to understand the complete gravity effect of dislocation sources, which is affected by the displacement of the free surface and the internal layer interfaces, but also by the elastic deformation of the continuum.

5 DISCUSSION AND CONCLUSIONS

We present a hybrid method for stable and efficient computations of complete synthetic seismograms based on a spherically symmetric and self-gravitating Earth model with a typical structure of the atmosphere, ocean, mantle, liquid core and solid core. For large wavelengths, a numerical scheme is used to solve the geodynamic boundary-value problem without any approximation on the deformation and gravity coupling. With the decreasing wavelength, the gravity effect on the deformation becomes negligible and the analytical propagator scheme can be used. In particular, we propose the useful approaches to overcome the degeneration problems, which may arise when using the analytical solutions, and the loss-of-precision problems which may arise in both analytical and numerical schemes.

Based on the hybrid method, an all-in-one code QSSP was implemented, which can be used for simulating body waves, surface waves, tsunami waves, infrasound gravity waves, free oscillations, and near-field static deformation caused by earthquakes. On a modern personal PC, complete synthetic seismograms can be easily calculated at the global scale for frequencies of up to 2 Hz. By using a narrow slowness window, body wave seismograms of even higher frequency (up to 5 Hz) can be simulated, too.

The performance of the code QSSP is demonstrated by various tests. One interesting test is to estimate the free oscillation mode S_1 , which is known as the Slichter mode, based on the Earth model PREM. It is found that if the Slichter mode could be caused by the 2004 M_w 9.3 Sumatra earthquake, its maximum amplitude for the gravity change on the Earth surface is about a quarter of one nGal that is at least one order smaller than what can be resolved by a modern superconducting gravimeter. In another test, tsunami and infrasound waves and the atmospheric and oceanic free oscillations are simulated. It should be emphasized that these simulations are based on spherically symmetric and non-rotating Earth models. In practice, the laterally heterogeneous bathymetry, wind and the effect of the Coriolis force make it difficult to observe the individual free oscillation modes of the real atmosphere and ocean. Nevertheless, the results from such simulations are helpful for understanding the physical basis for the mechanical (gravitational) coupling between the different subsystems of the Earth.

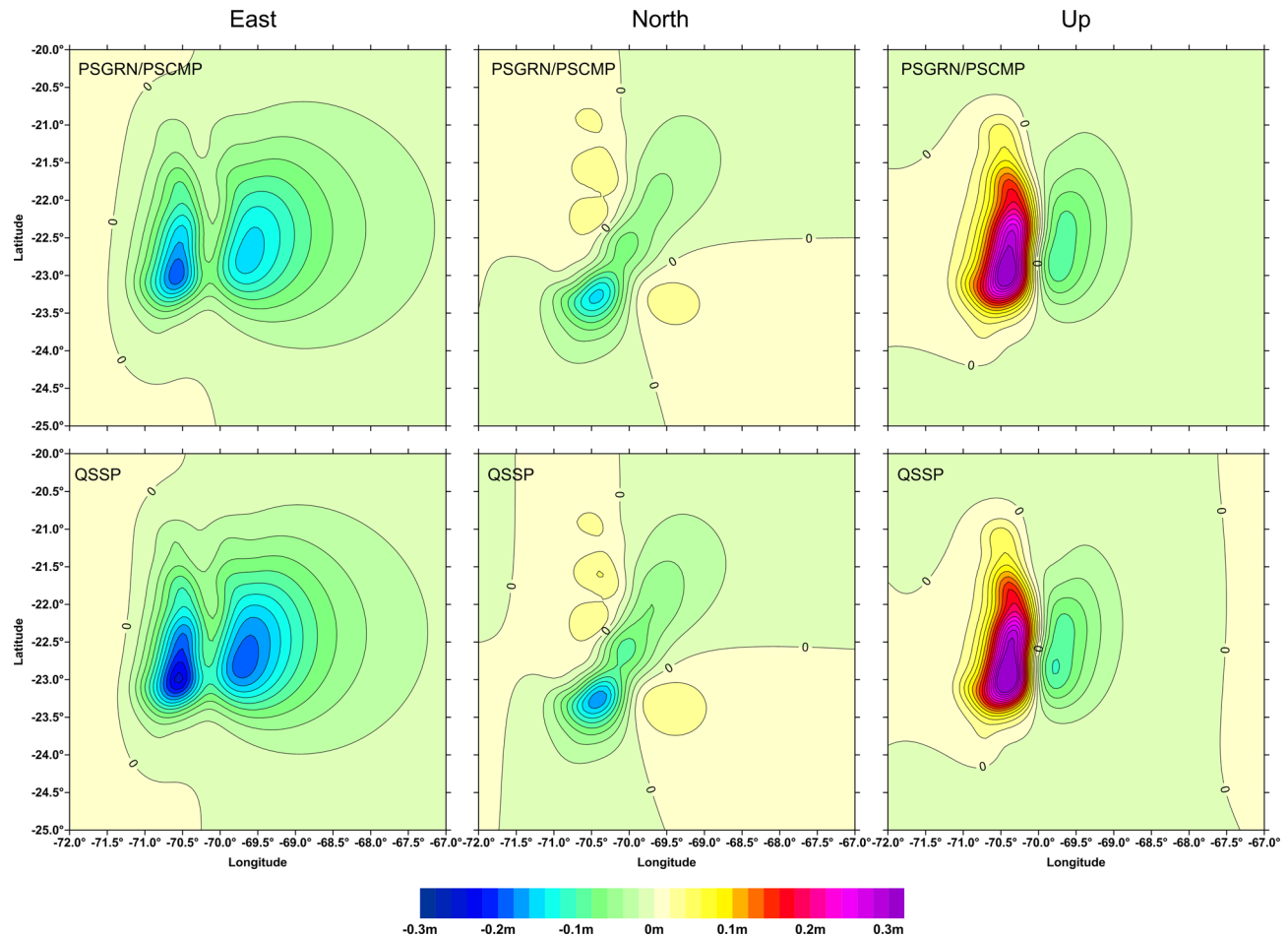


Figure 8. Comparison of the static surface displacement fields for the 2007 M_w 7.7 Tocopilla (Chile) earthquake calculated using two different codes QSSP (this study) and PSGRN/PSCMP (Wang *et al.* 2006). The Earth model used is AK135. The slip model of the earthquake consists of about 1000 fault patches adopted from Motagh *et al.* (2010).

QSSP is useful for the study of long period surface waves as well as for high-frequency body waves which travel through the outer and inner core and experience multiple reflections and scattering in the Earth. It is also useful for various kinds of source studies, from point source moment tensor inversion to slip imaging on the rupture plane of major earthquakes, especially if different types of seismic, geodetic, oceanic and engineering data are inverted simultaneously. The original QSSP as a stand-alone FORTRAN code can be downloaded from <ftp://ftp.gfz-potsdam.de/pub/home/turk/wang/>. The source inversion problem is supported by means of global and regional pre-calculated Green's function databases based on QSSP, which are provided as a community service at (<http://kinherd.org/>) or can be calculated individually using the Python toolbox Fomosto (<http://pyrocko.org/>). On the other hand, the high-precision results of QSSP can provide an ideal reference for global 3-D modelling using, for example the spectral-element method (Komatitsch & Tromp 1999).

In summary, the advantage of the all-in-one code QSSP is the use of a uniform algorithm based on a solid and well established theory. Therefore, bugs can be easily detected and modelling errors can be minimized. Additionally, with a small extension the QSSP can be used for modelling viscoelastic post-seismic deformation or postglacial rebound problems. The corresponding stand-alone FORTRAN code (QSSPSTATIC) is free available on the web, too.

ACKNOWLEDGEMENTS

The basic theory, approach and code of QSSP were developed over more than one decade by the first author alone. The co-authors contributed in terms of theory and code verification and testing, improvements, implementation of interfaces, examples and manuscript preparation. However, many other scientists and students who worked with QSSP have helped by providing feedback or formulating requests for further consideration. The authors thank Walter Zürn and another anonymous reviewer for their valuable comments.

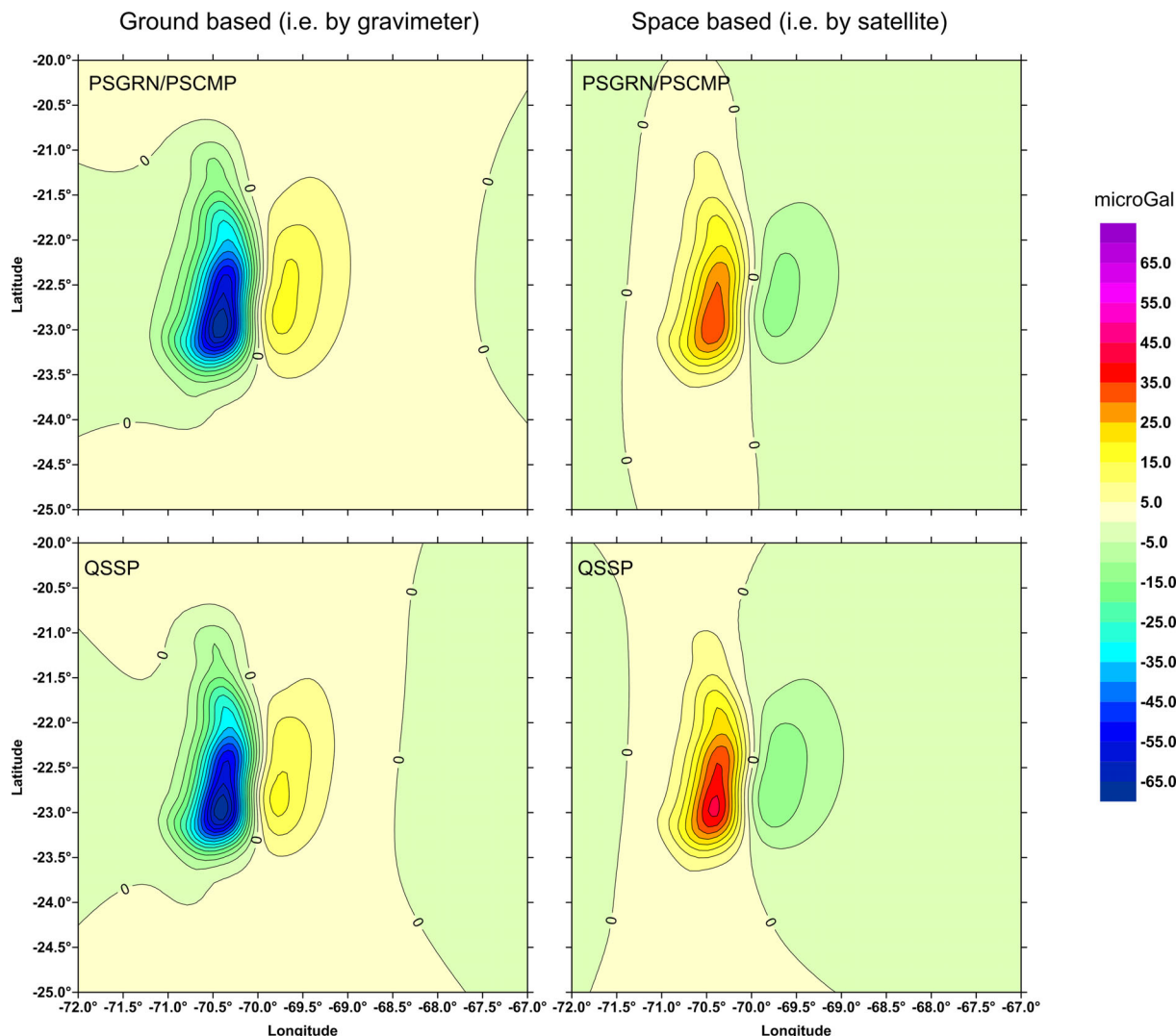


Figure 9. Same as Fig. 8, but for changes in the gravity field. Note that the difference between the ground and space based gravity changes is given by the free-air correction $\delta g_f = -\frac{2}{R} g_o u_r$, where R is Earth's radius, g_o is Earth's surface gravity, and u_r is the vertical surface displacement.

REFERENCES

- Al-Attar, D. & Woodhouse, J.H., 2008. Calculation of seismic displacement fields in self-gravitating earth models - applications of minors vectors and symplectic structure, *Geophys. J. Int.*, **175**, 1176–1208.
- Bouchon, M., 1979. Discrete wave number representation of elastic wave fields in three space dimensions, *J. geophys. Res.*, **84**, 3609–3614.
- Chapman, C.H., 2003. Yet another elastic plane-wave, layer-matrix algorithm, *Geophys. J. Int.*, **154**, 212–223.
- Chapman, C.H. & Phinney, R.A., 1972. Diffracted seismic signals and their numerical solution, *Meth. Comp. Phys.*, **12**, 165–230.
- Crossley, D.J., 1993. Eigensolutions and seismic excitation of the Slichter mode triplet for a fully rotating earth model, *EOS*, **73**, 60.
- Crossley, D., Rochester, M.J. & Peng, Z.R., 1992. Slichter modes and Love numbers, *Geophys. Res. Lett.*, **91**, 755–794.
- Dahlen, F.A., 1968. The normal modes of a rotating, elliptical Earth, *Geophys. J. R. astr. Soc.*, **16**, 329–367.
- Dahlen, F.A., 1972. Elastic dislocation theory for a self-gravitating elastic configuration with an initial static stress field, *Geophys. J. R. astron. Soc.*, **28**, 357–383.
- Dahlen, F.A. & Sailor, R., 1979. Rotational and elliptical splitting of the free oscillations of the earth, *Geophys. J. R. astr. Soc.*, **58**, 609–623.
- Dahlen, F.A. & Tromp, J., 1998. *Theoretical Global Seismology*, Princeton Univ. Press.
- Ding, H. & Chao, B.F., 2015. The Slichter mode of the Earth: revisit with optimal stacking and autoregressive methods on full superconducting gravimeter data set, *J. geophys. Res.*, **120**, 7261–7272.
- Dziewonski, A.M. & Anderson, D.L., 1981. Preliminary reference Earth model, *Phys. Earth planet. Inter.*, **25**, 297–356.
- Dunkin, J.W., 1965. Computation of modal solutions in layered, elastic media at high frequencies, *Bull. seism. Soc. Am.*, **55**, 335–358.
- Friederich, W. & Dalkolmo, J., 1995. Complete synthetic seismograms for a spherically symmetric earth by a numerical computation of Green's function in the frequency domain, *Geophys. J. Int.*, **122**, 537–550.
- Fuchs, K., 1968. The reflection of spherical waves from transition zones with arbitrary depth-dependent elastic moduli and density, *J. Phys. Earth*, **16**, 27–41.
- Fuchs, K. & Müller, G., 1971. Computation of synthetic seismograms with the reflectivity method and comparison with observation, *Geophys. J. R. astr. Soc.*, **23**, 417–433.
- Gilbert, F. & Backus, G., 1966. Propagator matrices in elastic wave and vibration problems, *Geophysics*, **31**, 326–332.
- Gilbert, F. & Backus, G., 1968. Elastic-gravitational vibrations of a radially stratified sphere, in *Dynamics of Stratified Solids*, pp. 82–95 ed. Herrmann, G., American Society of Mechanical Engineers, New York.
- Heimann, S., González, Á., Wang, R., Cesca, S. & Dahm, T., 2013. Seismic characterization of the Chelyabinsk meteor's terminal explosion, *Seism. Res. Lett.*, **84**, 1021–1025.

- Hinderer, J., Crossley, D. & Jensen, O., 1995. A search for the Slichter triplet in superconducting gravimeter data, *Phys. Earth planet. Inter.*, **90**, 183–195.
- Hoechner, A., Babeyko, A.Y. & Sobolev, S.V., 2008. Enhanced GPS inversion technique applied to the 2004 Sumatra earthquake and tsunami, *Geophys. Res. Lett.*, **35**, L08310, doi:10.1029/2007GL033133.
- Ivan, M. & Wang, R., 2013. Anomalous high amplitude ratios of P5KP/PKPa and P4KP/P(S)cP observed globally around 1 Hz, *J. Seismol.*, **17**, 453–464.
- Ivan, M., Ghica, D.V., Gosar, A., Hatzidimitriou, P., Hofstetter, R., Polat, G. & Wang, R., 2015. Lowermost mantle velocity estimations beneath the central North Atlantic area from PdPf observed at Balkan, East Mediterranean, and American stations, *Pure appl. Geophys.*, **172**, 283–293.
- Kanamori, H. & Anderson, D.L., 1977. Importance of physical dispersion in surface waves and free oscillation problems, *Rev. Geophys. Space Phys.*, **15**, 105–112.
- Kanamori, H. & Rivera, L., 2008. Source inversion of *W* phase: speeding up seismic tsunami warning, *Geophys. J. Int.*, **175**, 222–238.
- Kawai, K., Takeuchi, N. & Geller, R.J., 2006. Complete synthetic seismograms up to 2 Hz for transversely isotropic spherically symmetric media, *Geophys. J. Int.*, **164**, 411–424.
- Kennett, B.L.N., 1983. *Seismic Wave Propagation in Stratified Media*, Cambridge Univ. Press.
- Kennett, B.L.N., Engdahl, E.R. & Buland, R., 1995. Constraints on seismic velocities in the Earth from travel times, *Geophys. J. Int.*, **122**, 108–124.
- Kind, R., 1983. Improvements to layer matrix method, *J. Geophys.*, **53**, 127–130.
- Knopoff, L., 1964. A matrix method for elastic wave problems, *Bull. seism. Soc. Am.*, **54**, 431–438.
- Komatitsch, D. & Tromp, J., 1999. Introduction to the spectral-element method for 3-D seismic wave propagation, *Geophys. J. Int.*, **139**, 806–822.
- Lognonné, P., Clévéde, E. & Kanamori, H., 1998. Computation of seismograms and atmospheric oscillations by normal mode summation for a spherical Earth model with realistic atmosphere, *Geophys. J. Int.*, **135**, 388–406.
- Ma, Y., Wang, R. & Zhou, H., 2012. A note on the equivalence of three major propagator algorithms for computational stability and efficiency, *Earthq. Sci.*, **25**, 55–64.
- Masters, G., Barmine, M. & Kientz, S., 2011. *Mineos – User Manual Version 1.0.2*, www.geodynamics.org.
- Motagh, M., Schurr, B., Anderssohn, J., Cailleau, B., Walter, T.R., Wang, R. & Villotte, J.P., 2010. Subduction earthquake deformation associated with 14 November 2007, Mw 7.8 Tocopilla earthquake in Chile: Results from InSAR and aftershocks, *Tectonophysics*, **490**, 60–68.
- Müller, G., 1977. Earth-flattening approximation for body waves derived from geometric ray theory - improvements, corrections and range of applicability, *J. Geophys.*, **42**, 429–436.
- Müller, G., 1983. Rheological properties and velocity dispersion of a medium with a power-law dependence of Q on frequency, *J. Geophys.*, **54**, 20–29.
- Müller, G., 1985. The reflectivity method: a tutorial, *J. Geophys.*, **58**, 153–174.
- Ochi, Y. et al., 2000. Global superconducting gravimeter observations and the search for the translational modes of the inner core, *Phys. Earth planet. Inter.*, **117**, 3–20.
- Okada, Y., 1992. Internal deformation due to shear and tensile faults in a half-space, *Bull. seism. Soc. Am.*, **82**, 1018–1040.
- Okubo, S., 1993. Reciprocity theorem to compute the static deformation due to a point dislocation buried in a spherically symmetric earth, *Geophys. J. Int.*, **115**, 921–928.
- Peng, Z.R., 1997. Effects of a mushy transition zone at the inner core boundary on the Slichter modes, *Geophys. J. Int.*, **131**, 607–617.
- Pollitz, F.F., 1992. Postseismic relaxation theory on the spherical Earth, *Bull. seism. Soc. Am.*, **82**, 422–453.
- Pollitz, F.F., 1997. Gravitational viscoelastic postseismic relaxation on a layered spherical earth, *J. geophys. Res.*, **102**, 17 921–17 941.
- Raveloson, A., Wang, R., Kind, R., Ceranna, L. & Yuan, X., 2012. Brief communication ‘Seismic and acoustic-gravity signals from the source of the 2004 Indian Ocean Tsunami’, *Nat. Hazards Earth Syst. Sci.*, **12**, 287–294.
- Rieutord, M., 2002. Slichter modes of the Earth revisited, *Phys. Earth planet. Inter.*, **131**, 269–278.
- Rochester, M.G. & Peng, Z.R., 1993. The Slichter modes of the rotating Earth: a test of the subseismic approximation, *Geophys. J. Int.*, **113**, 575–585.
- Roister, Y., 2003. Splitting of seismic-free oscillations and of the Slichter triplet using the normal mode theory of a rotating, ellipsoidal Earth, *Phys. Earth planet. Inter.*, **140**, 169–182.
- Rosat, S., Roister, Y., Crossley, D. & Hinderer, J., 2006. A search for the Slichter triplet with superconducting gravimeters: Impact of the density jump at the inner core boundary, *J. Geodyn.*, **41**, 296–306.
- Rundle, J.B., 1980. Static elastic-gravitational deformation of a layered half-space by point couple sources, *J. geophys. Res.*, **85**, 5354–5363.
- Rundle, J.B., 1981. Vertical displacements from a rectangular fault in a layered elastic-gravitational media, *J. Phys. Earth*, **29**, 173–186.
- Rundle, J.B., 1982. Viscoelastic-gravitational deformation by a rectangular thrust fault in a layered Earth, *J. geophys. Res.*, **87**, 7787–7796.
- Schurr, B. et al., 2014. Gradual unlocking of plate boundary controlled initiation of the 2014 Iquique earthquake, *Nature*, **512**, 299–302.
- Segall, P., 2010. *Earthquake and Volcano Deformation*, Princeton Univ. Press.
- Slichter, L.B., 1961. The fundamental free mode of the Earth’s inner core, *Proc. Natl. Acad. Sci. U.S.A.*, **47**, 186–190.
- Sun, W. & Okubo, S., 1993. Surface potential and gravity changes due to internal dislocations in a spherical earth - I. Theory for a point dislocation, *Geophys. J. Int.*, **114**, 569–592.
- Sun, W. & Okubo, S., 1998. Surface potential and gravity changes due to internal dislocations in a spherical earth - II. Application to a finite fault, *Geophys. J. Int.*, **132**, 79–88.
- Takeuchi, H. & Saito, M., 1972. Seismic surface waves, in *Methods in Computational Physics*, pp. 217–295, ed. Bolt, B.A., Academic Press, New York.
- Tong, X. et al., 2010. The 2010 Maule, Chile earthquake: Downdip rupture limit revealed by space geodesy, *Geophys. Res. Lett.*, **37**, L24311, doi:10.1029/2010GL045805.
- van Driel, M., Krischer, L., Stähler, S.C., Hosseini, K. & Nissen-Meyer, T., 2015. Instaseis: instant global seismograms based on a broadband waveform database, *Solid Earth*, **6**, 701–717.
- Wang, R., 1991. *Tidal Deformations on a Rotating, Spherically Asymmetric, Viscoelastic and Laterally Heterogeneous Earth*, European University Studies, Series XVII, Earth Sciences, Vol. 5, Peter Lang, Frankfurt am Main.
- Wang, R., 1997. Tidal response of the solid earth, in *Tidal Phenomena, Lecture Notes in Earth Sciences*, Vol. 66, pp. 27–57, ed. Wilhelm, H., Zürn, W. & Wenzel, H.G., Springer-Verlag, Berlin/Heidelberg, Germany.
- Wang, R., 1999. A simple orthonormalization method for stable and efficient computation of Green’s functions, *Bull. seism. Soc. Am.*, **89**, 733–741.
- Wang, R., Lorenzo Martín, F. & Roth, F., 2003. Computation of deformation induced by earthquakes in a multi-layered elastic crust - FORTRAN programs EDGRN/EDCMP, *Comput. Geosci.*, **29**, 195–207.
- Wang, R. & Kümpel, H.J., 2003. Poroelasticity: Efficient modelling of strongly coupled, slow deformation processes in a multilayered half-space, *Geophysics*, **68**, 705–717.
- Wang, R., Lorenzo Martín, F. & Roth, F., 2006. PSGRN/PSCMP - a new code for calculating co- and post-seismic deformation, geoid and gravity changes based on the viscoelastic gravitational dislocation theory, *Comput. Geosci.*, **32**, 527–541.
- Wang, R. & Wang, H., 2007. A fast converging and anti-aliasing algorithm for Green’s functions in terms of spherical or cylindrical harmonics, *Geophys. J. Int.*, **170**, 239–248.
- Yang, H.Y., Zhao, L. & Hung, S.H., 2010. Synthetic seismograms by normal-mode summation: a new derivation and numerical examples, *Geophys. J. Int.*, **183**, 1613–1632.

Zhang, Y., Wang, R., Zschau, J., Chen, Y.T., Parolai, S. & Dahm, T., 2014a. Automatic imaging of earthquake rupture processes by iterative deconvolution and stacking of high-rate GPS and strong motion seismograms, *J. geophys. Res.*, **119**, 5633–5650.

Zhang, Y., Wang, R., Chen, Y.T., Xu, L., Du, F., Jin, M., Tu, H. & Dahm, T., 2014b. Kinematic rupture model and hypocenter relocation of the 2013 Mw6.6 Lushan earthquake constrained by strong-motion and teleseismic data, *Seism. Res. Lett.*, **85**, 15–22.

SUPPORTING INFORMATION

Supplementary data are available at [GJI](#) online.

Figure S1. Example of time-domain aliasing. The synthetic seismograms are calculated using the seismic reference model AK135 with a point dislocation source located close to the free surface. The frequency and slowness cut-offs are uniformly set to 1.0 Hz and 0.25 s km⁻¹, respectively, while the suppression factor for the time-domain aliasing $e^{-\sigma T}$ [see eq. (31) in the main text] is set to 0.99 for the red traces and 0.01 for the blue traces.

Figure S2. Comparison between the original and differentially transformed harmonic spectra of the synthetic seismograms shown in Fig. S1, both truncated sharply at $l = 2000$, corresponding to a slowness cut-off at 0.10 s km⁻¹ (dashed lines). The red curve shows the real part of the original harmonic coefficients that were used to synthesize the seismograms shown in Fig. S1, compared with the blue curve showing the fourth-order differential transform (see eq. 34) of the former.

Figure S3. Example of space-domain aliasing. As shown in Section 3.3 of the main text, complete seismograms can be synthesize alternatively using the original harmonic coefficients (see eq. 33 in the main text) and the differentially transformed harmonic coefficients (see eq. 34 in the main text). However, once a narrow slowness window is used to filter slow phases like S or surface waves, the use of the differential transform can efficiently suppress the space-domain aliasing caused by the sharp slowness cut-off. Here the red and blue traces are synthetic seismograms obtained using the original and differential transformed spectra shown in Fig. S2, respectively. The space-domain aliasing, also called numerical phases, appear only in the red traces and travel exactly with the cut-off slowness of ± 0.1 s km⁻¹ (or velocity of ± 10 km s⁻¹).

Figure S4. Example of high-frequency core phases calculated for a simple two-layer earth model. The code QSSP is able to filter the free-surface reflection and waves with shallow turning points. In this example, the model consists of a homogeneous solid sphere with a homogeneous liquid core. By filtering the free-surface reflection, the model is equivalent to a homogeneous full space with a homogeneous liquid core. Additionally by filtering the waves with turning points shallower than the core boundary, only the core phases are remaining, all of which can be easily identified using seismic ray theory (labelled by red).

Figure S5. Similar to Fig. S1, but for the seismic reference Earth model AK135. The red dotted lines show the core phases PmKP ($m \leq 4$) within the time window of 3000 s based on the ray theory.

Figure S6. Same as Fig. S5, but for time window 3000–6000 s. Note that the AB (AB_{diff}) branches of PmKP ($m > 4$) are clearly visible, while the corresponding AB branches (dotted red lines according to the ray theory) are invisible in the synthetic seismograms.

Figure S7. Waveform and relative amplitude of the core phases PmKP ($m \leq 7$) shown in Figs S5 and S6. The epicentral distances for which the core phases are calculated are given in the parentheses.

Figure S8. Record section of long period W-phases (Z-component) between 25° and 85°, calculated for an explosion source in 20 km depth. The indicated W-phase window is selected according to Kanamori & Rivera (2008). The data are filtered between 1 and 5 mHz and were scaled to their maximum within the W-phase window. The blue traces [$a(t)$] are calculated for a self-gravitational Earth, whereas the red ones [$a^e(t)$] were calculated by neglecting gravity. The numbers on the right give the residuals calculated within the W-phase time window by $r = \sqrt{\sum (a_i - a_i^e)^2 / a_i^2}$.

Table S1. Comparison of low-frequency (≤ 2 mHz) normal modes calculated using two different codes MINEOS and QSSP. The model used is the effective isotropic version of Earth model PREM (Dziewanski & Anderson 1981), in which the 3 km ocean layer is replaced by the solid medium of the upper crust. The inner core translational mode ${}_1S_1$, also called Slichter mode, cannot be provided by the version of MINEOS used in this study. The differences between the results (particularly the Q values) of all other modes calculated by MINEOS and QSSP are probably caused by the different numerical approach used in MINEOS to determine the attenuation effect. Actually, MINEOS calculates the normal modes in two steps. First the eigenfrequency and eigenfunction are determined for a purely elastic earth model without attenuation. Then the quality factor (or the imaginary part of eigenfrequency) and its effect on the eigenfrequency are estimated based on the perturbation theory. In contrast, QSSP determines the eigenfrequency and quality factor simultaneously using the correspondence principle without any approximation.

Please note: Oxford University Press is not responsible for the content or functionality of any supporting materials supplied by the authors. Any queries (other than missing material) should be directed to the corresponding author for the paper.

APPENDIX A: DESCRIPTION OF THE GEODYNAMIC BOUNDARY-VALUE PROBLEM BASED ON A SPHERICALLY SYMMETRIC, ISOTROPIC LINEAR ELASTIC AND SELF-GRAVITATING EARTH MODEL

Assume an infinitesimal dynamic deformation process superposed on the initial hydrostatic equilibrium of a spherically symmetric, elastic and self-gravitating Earth. Using the spherical co-ordinate system (r, θ, φ) with the origin ($r = 0$) at the Earth mass centre, the frequency-domain

equations of motion governing the infinitesimal deformation is written in the form,

$$\begin{cases} -\rho\omega^2\mathbf{u} = \nabla \cdot \boldsymbol{\sigma} + \rho\nabla(\psi - gu_r) + \rho g(\nabla \cdot \mathbf{u})\mathbf{e}_r + \mathbf{f}, \\ \nabla^2\psi = 4\pi G\nabla \cdot (\rho\mathbf{u}), \end{cases} \quad (\text{A1})$$

(see, e.g. Dahlen 1972), where ω is the angular frequency, $\rho = \rho(r)$ is the density, G is the gravitational constant, $\mathbf{f} = \mathbf{f}(r, \theta, \varphi)$ is the body force (seismic source), $\mathbf{u} = \mathbf{u}(r, \theta, \varphi)$ is the particle displacement vector, $\psi = \psi(r, \theta, \varphi)$ is the incremental gravity potential, $\boldsymbol{\sigma} = \boldsymbol{\sigma}(r, \theta, \varphi)$ is the incremental stress tensor, and $g = g(r)$ is the Earth gravity (downwards positive),

$$g(r) = \frac{4\pi G}{r^2} \int_0^r \rho(\xi)\xi^2 d\xi. \quad (\text{A2})$$

For the interested reader, we notice that in the above equations, $\boldsymbol{\sigma}$ is the incremental stress tensor in the Lagrangian (or material) description, whereas ψ is the incremental gravity potential in the Eulerian (or spatial) description. The choice of this mixed description is for the reason that the constitutive law relating the stress to strain is material based, but the local gravity potential is commonly used in the space geodesy. Additionally, the mixed description leads to a simple form of the boundary conditions (Wang 1997).

For the isotropic, linear elastic medium, the stress tensor is related to the strain tensor by Hooke's law,

$$\boldsymbol{\sigma} = \lambda(\nabla \cdot \mathbf{u})\mathbf{I} + \mu[\nabla\mathbf{u} + (\nabla\mathbf{u})^T], \quad (\text{A3})$$

where \mathbf{I} is the unit tensor, and $\lambda = \lambda(r)$ and $\mu = \mu(r)$ are the two Lamé constants.

At an interior interface $r = r_i$, the displacement, stress and potential satisfy in general the following continuity conditions,

$$\begin{cases} \mathbf{u}|_+^+ = \mathbf{0}, \\ \mathbf{e}_r \cdot \boldsymbol{\sigma}|_+^+ = \mathbf{0}, \\ \psi|_+^+ = 0, \\ \mathbf{e}_r \cdot (\nabla\psi - 4\pi G\rho\mathbf{u})|_+^+ = 0, \end{cases} \quad (\text{A4})$$

where $\mathbf{u}|_+^+ = \mathbf{u}(r_i^+, \theta, \varphi) - \mathbf{u}(r_i^-, \theta, \varphi)$ denotes the jump of displacement through the interface, and so on. If the interface is frictionless, for example, at the boundary between the core and mantle or between the inner core and outer core, the displacement continuity is required only for its normal component, that is $\mathbf{u}|_+^+ = \mathbf{0}$ is replaced by $u_r|_+^+ = 0$ in this case. At the Earth centre, the regularity conditions are required,

$$\begin{cases} \mathbf{u}|_{r \rightarrow 0} < \infty, \\ \mathbf{e}_r \cdot \nabla\psi|_{r \rightarrow 0} < \infty. \end{cases} \quad (\text{A5})$$

The free surface conditions are expressed by

$$\begin{cases} \mathbf{e}_r \cdot \boldsymbol{\sigma}|_{r=a} = \mathbf{0}, \\ \mathbf{e}_r \cdot (\nabla\psi - 4\pi G\rho\mathbf{u})|_{r=a} = 0. \end{cases} \quad (\text{A6})$$

where a is the Earth radius, and in the mass-free external space, the potential is required to be harmonic.

In the spectral method, the frequency-domain field quantities are expanded in terms of vector spherical harmonics,

$$\begin{cases} \mathbf{u} = \sum_{l=0}^{\infty} \sum_{m=-l}^l [U_l^m(r) \mathbf{R}_l^m(\theta, \varphi) + V_l^m(r) \mathbf{S}_l^m(\theta, \varphi) + W_l^m(r) \mathbf{T}_l^m(\theta, \varphi)], \\ \psi = \sum_{l=0}^{\infty} \sum_{m=-l}^l \Phi_l^m(r) Y_l^m(\theta, \varphi), \\ \mathbf{e}_r \cdot \boldsymbol{\sigma} = \sum_{l=0}^{\infty} \sum_{m=-l}^l [E_l^m(r) \mathbf{R}_l^m(\theta, \varphi) + F_l^m(r) \mathbf{S}_l^m(\theta, \varphi) + G_l^m(r) \mathbf{T}_l^m(\theta, \varphi)], \end{cases} \quad (\text{A7})$$

where

$$\begin{cases} \mathbf{R}_l^m(\theta, \varphi) = \mathbf{e}_r Y_l^m(\theta, \varphi), \\ \mathbf{S}_l^m(\theta, \varphi) = \mathbf{e}_\theta \frac{\partial}{\partial\theta} Y_l^m(\theta, \varphi) + \mathbf{e}_\varphi \frac{1}{\sin\theta} \frac{\partial}{\partial\varphi} Y_l^m(\theta, \varphi), \\ \mathbf{T}_l^m(\theta, \varphi) = \mathbf{e}_\theta \frac{1}{\sin\theta} \frac{\partial}{\partial\varphi} Y_l^m(\theta, \varphi) - \mathbf{e}_\varphi \frac{\partial}{\partial\theta} Y_l^m(\theta, \varphi), \end{cases} \quad (\text{A8})$$

and

$$Y_l^m(\theta, \varphi) = P_l^{|m|}(\cos\theta) e^{im\varphi}, \quad (\text{A9})$$

are the spherical surface functions and $P_l^{|m|}(\cos \theta)$ the associated Legendre polynomials of degree l and order m . Note that, if synthetic Green's functions are calculated for typical seismic sources, that is, a single force or a point dislocation, $|m|$ only takes 0, 1 and 2.

Using the completeness and orthogonality of the spherical surface functions, the partial differential equations of motion eq. (A1) can be converted to a system of ordinary differential equations governing the expansion coefficients in eq. (A7). Thus, the toroidal mode is described by a generalized 2-D displacement-stress vector,

$$\mathbf{X} = (W_l^m, G_l^m)^T, \quad (\text{A10})$$

and the spheroidal mode by a generalized 6-D displacement-stress vector,

$$\mathbf{y} = \left(U_l^m, E_l^m, V_l^m, F_l^m, \Phi_l^m, \dot{\Phi}_l^m + \frac{l+1}{r} \Phi_l^m - 4\pi G\rho U_l^m \right)^T, \quad (\text{A11})$$

where the dot denotes the derivative with respect to r .

In the case of the spherical symmetry, the two different modes are decoupled from each other and therefore can be solved independently. The ordinary differential equations of motion governing the toroidal mode is given by

$$\begin{cases} \dot{X}_1 = \frac{1}{r} X_1 + \frac{1}{\mu} X_2, \\ \dot{X}_2 = \left[-\rho\omega^2 + \frac{(l-1)(l+2)\mu}{r^2} \right] X_1 - \frac{3}{r} X_2. \end{cases} \quad (\text{A12})$$

For a homogeneous spherical shell, eq. (A12) can be solved analytically. There exist two fundamental toroidal solutions, which are given in the main text.

The ordinary differential equations of motion governing the spheroidal mode is given by

$$\begin{cases} \dot{Y}_1 = -\frac{2\lambda}{(\lambda+2\mu)r} Y_1 + \frac{1}{\lambda+2\mu} Y_2 + \frac{l(l+1)\lambda}{(\lambda+2\mu)r} Y_3, \\ \dot{Y}_2 = \left[-\rho\omega^2 - \frac{4\rho g}{r} + \frac{4\mu(3\lambda+2\mu)}{(\lambda+2\mu)r^2} \right] Y_1 - \frac{4\mu}{(\lambda+2\mu)r} Y_2 + l(l+1) \left[\frac{\rho g}{r} - \frac{2\mu(3\lambda+2\mu)}{(\lambda+2\mu)r^2} \right] Y_3 + \frac{l(l+1)}{r} Y_4 + \frac{(l+1)\rho}{r} Y_5 - \rho Y_6, \\ \dot{Y}_3 = -\frac{1}{r} Y_1 + \frac{1}{r} Y_3 + \frac{1}{\mu} Y_4, \\ \dot{Y}_4 = \left[\frac{\rho g}{r} - \frac{2\mu(3\lambda+2\mu)}{(\lambda+2\mu)r^2} \right] Y_1 - \frac{\lambda}{(\lambda+2\mu)r} Y_2 + \left\{ -\rho\omega^2 + \frac{2\mu}{r^2} \left[\frac{2l(l+1)(\lambda+\mu)}{\lambda+2\mu} - 1 \right] \right\} Y_3 - \frac{3}{r} Y_4 - \frac{\rho}{r} Y_5, \\ \dot{Y}_5 = 4\pi G\rho Y_1 - \frac{l+1}{r} Y_5 + Y_6, \\ \dot{Y}_6 = \frac{4\pi G\rho(l+1)}{r} Y_1 - \frac{4\pi G\rho l(l+1)}{r} Y_3 + \frac{l-1}{r} Y_6. \end{cases} \quad (\text{A13})$$

Note that due to the spherical symmetry, the harmonic order m does not appear in the above equations of motion. The dependence of the expansion coefficients on m is fully determined by the radiation pattern of the source used.

Two special cases need to be noted. The first one is for $l = 0$. In this case, the toroidal mode is meaningless and it can be derived that $Y_6 = Y_5/r$ for the spheroidal mode. Accordingly, eq. (A13) is reduced to a 3-D equation system including Y_1 , Y_2 and Y_5 ,

$$\begin{cases} \dot{Y}_1 = -\frac{2\lambda}{(\lambda+2\mu)r} Y_1 + \frac{1}{\lambda+2\mu} Y_2, \\ \dot{Y}_2 = \left[-\rho\omega^2 - \frac{4\rho g}{r} + \frac{4\mu(3\lambda+2\mu)}{(\lambda+2\mu)r^2} \right] Y_1 - \frac{4\mu}{(\lambda+2\mu)r} Y_2, \\ \dot{Y}_5 = 4\pi G\rho Y_1. \end{cases} \quad (\text{A14})$$

Note that Y_5 is hierarchically coupled with Y_1 and Y_2 in eq. (A14). Accordingly, Y_1 and Y_2 be solved independently from Y_5 .

The other special case is for $\mu = 0$, that is for a liquid medium such as the outer core, the ocean or the atmosphere, where the shear stress vanishes ($Y_4 = 0$) and the toroidal mode does not exist (no shear waves). According to eq. (A13), the vanishing of μ and Y_4 leads to the relation

$$\rho g Y_1 - Y_2 - \rho\omega^2 r Y_3 - \rho Y_5 = 0, \quad (\text{A15})$$

and the 6-D equation system governing the spheroidal modes is simplified to a 4-D equation system,

$$\begin{cases} \dot{Y}_1 = -\frac{2}{r} Y_1 + \frac{1}{\lambda} Y_2 + \frac{l(l+1)}{r} Y_3, \\ \dot{Y}_2 = -\left(\rho\omega^2 + \frac{4\rho g}{r}\right) Y_1 + \frac{l(l+1)\rho g}{r} Y_3 + \frac{(l+1)\rho}{r} Y_5 - \rho Y_6, \\ \dot{Y}_5 = 4\pi G\rho Y_1 - \frac{l+1}{r} Y_5 + Y_6, \\ \dot{Y}_6 = \frac{4\pi G\rho(l+1)}{r} Y_1 - \frac{4\pi G\rho l(l+1)}{r} Y_3 + \frac{l-1}{r} Y_6, \end{cases} \quad (\text{A16})$$

where Y_3 is related to Y_1 , Y_2 and Y_5 through eq. (A15). Note that, at the static limit, that is when $\omega \rightarrow 0$, eq. (A16) becomes generally unstable because ω appears in the denominator of several terms if substituting Y_3 by eq. (A15). To overcome the problem, Wang (1991) suggested an alternative equation system, which can be obtained by differentiating eq. (A15). This new equation system includes Y_1 , Y_3 , Y_5 and Y_6 as the independent unknowns,

$$\begin{cases} \dot{Y}_1 = \left(\frac{\rho g}{\lambda} - \frac{2}{r}\right) Y_1 + \left[\frac{l(l+1)}{r} - \frac{\rho\omega^2 r}{\lambda}\right] Y_3 - \frac{\rho}{\lambda} Y_5, \\ \dot{Y}_3 = \frac{1}{r} \left(1 - \frac{N^2}{\omega^2}\right) Y_1 - \frac{1}{r} \left(1 - \frac{N^2 r}{g}\right) Y_3 + \frac{N^2}{\omega^2 g r} Y_5, \\ \dot{Y}_5 = 4\pi G\rho Y_1 - \frac{l+1}{r} Y_5 + Y_6, \\ \dot{Y}_6 = \frac{4\pi G\rho(l+1)}{r} Y_1 - \frac{4\pi G\rho l(l+1)}{r} Y_3 + \frac{l-1}{r} Y_6, \end{cases} \quad (\text{A17})$$

where

$$N^2 = -\frac{g}{\rho} \left(\frac{d\rho}{dr} + \frac{\rho^2 g}{\lambda} \right), \quad (\text{A18})$$

and $N/2\pi$ is the Brunt–Väisälä frequency. After Y_1 , Y_3 , Y_5 and Y_6 have been solved using eq. (A17), Y_2 is determined by eq. (A15). In the Earth outer core and ocean, the so-called Adam–Williamson condition, that is $N^2 = 0$, is approximately satisfied. In the Earth atmosphere, $N^2 > 0$ and the Brunt–Väisälä frequency ranges between 1.75 and 3.68 mHz based on the US standard model. It can be seen that generally no stable solution can be determined for eq. (A17) at the static limit. In practice, however, static deformation makes sense only within the solid Earth. For numerical convenience, one can modify N^2 so that it becomes frequency-dependent below a critical frequency f_o , which is equal to or smaller than the real Brunt–Väisälä frequency. For example,

$$N^2(f) = \begin{cases} N_o^2 \sin^{2+\alpha} \left(\frac{\pi f}{2f_o} \right), & \text{for } f < f_o, \\ N_o^2, & \text{for } f \geq f_o, \end{cases} \quad (\text{A19})$$

where $\alpha \geq 0$ and N_o^2 is calculated using eq. (A18). At the static limit, eq. (A17) becomes a stable system because the singularity caused by the terms including the ratio N^2/ω^2 is thereby avoided.

The boundary conditions to be satisfied by the generalized displacement–stress vector can be derived consistently from eqs (A4) to (A6). For each wedged solid to solid interface, the continuity condition is valid for all components of both toroidal and spheroidal displacement–stress vectors.

Since the toroidal motion can be excited only in a solid subsystem where the source is located, its boundary condition is given by $X_2 = 0$ at the free solid Earth surface, the core–mantle boundary and the inner core boundary.

For the spheroidal motion of degree $l = 0$, the displacement–stress vector is continuous everywhere. For $l > 0$, however, some attentions should be paid to the conditions at frictionless interfaces like from solid to liquid, from liquid to solid, or from liquid to liquid. In the propagator algorithm, it needs generally to propagate 3 independent displacement–stress vectors simultaneously through each solid layer and 2 through each liquid layer. At an interface from solid to liquid, the 3 vectors on the solid side are linearly combined to 2 vectors to satisfy the vanishing shear stress condition ($Y_4 = 0$). The latter 2 vectors will be propagated further in the liquid layer. At an interface from liquid to solid, the 2 vectors on the liquid side are continued to the solid side and a third vector will be generated in the form like $y = (0, 0, c, 0, 0, 0)^T$, where c is the third constant of integration representing a net jump in the horizontal displacement there. Finally, at an interface from liquid to liquid with density discontinuity, each of the 2 independent vectors should be allowed to include a jump in the horizontal displacement to satisfy the continuity condition of the normal stress given by eq. (A15).

In addition, a special attention should be paid to the boundary conditions for both toroidal and spheroidal motions of degree $l = 1$. In this case, the rigid rotation of the Earth and the translational motion of the centre of the Earth become unconstrained by the boundary conditions described above when $f \rightarrow 0$. Consequently, numerical instabilities may arise at very low frequencies. The difficulty can be overcome by using the centre of mass system, in which the law of conservation of linear and angular momentum is valid.

For the spheroidal motion of degree $l = 1$, one of the surface conditions, $Y_6(a) = 0$, needs to be modified to $Y_5(a) = 0$. For any internal force like an earthquake, $Y_5(a) = 0$ for degree degree $l = 1$ is a logical consequence in the centre of mass system and the two alternative surface conditions are equivalent. For an external force like a meteorite impaction, however, $Y_5(a)$ and $Y_6(a)$ cannot vanish simultaneously. If the condition $Y_5(a) = 0$ is chosen, it is generally expected that $Y_6(a) \neq 0$, implying that the centre of mass system is non-inertial under the external forcing.

Similarly, the rigid rotation should be avoided when calculating the toroidal motion of degree $l = 1$. In principle, only an external force can result in a net moment acting on the Earth, which is represented by a jump of shear stress (X_2) at the source level. In this case, the angular momentum is no more a conserved quantity. In the centre of mass system, it is therefore necessary to require the continuity of shear stress at the source level, or equivalently to require that

$$\int_0^a \rho r^3 X_1 dr = 0, \quad (\text{A20})$$

implying the conservation of angular momentum, where the integral can be carried out simultaneously with eq. (A12).